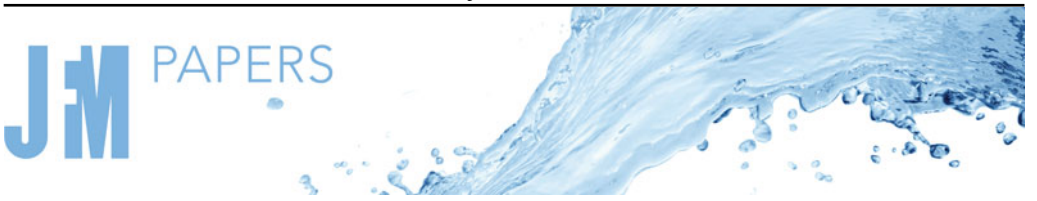
J. Fluid Mech. (2025), *vol.* 1023, A34, doi:10.1017/jfm.2025.10828



Hydrodynamic instability driven by two co-propagating shock waves across varying Atwood numbers

Yinuo Xing[1], **Zhiming Dong**[1], **He Wang**[1], **Zhigang Zhai**[1] and **Xisheng Luo**[1,2]

[1]Advanced Propulsion Laboratory, Department of Modern Mechanics, University of Science and Technology of China, Hefei 230026, PR China

[2]State Key Laboratory of High-Temperature Gas Dynamics, Institute of Mechanics, Chinese Academy of Sciences, Beijing 100190, PR China

Corresponding author: He Wang, ustchewang@ustc.edu.cn

(Received 19 April 2025; revised 10 August 2025; accepted 10 October 2025)

The evolution mechanisms and suppression strategy of the Richtmyer–Meshkov instability (RMI) at heavy–light interfaces with varying Atwood numbers accelerated by two co-propagating shock waves are investigated through theoretical analysis and experimental evaluation. Existing models describing the complete evolution of once-shocked interfaces and the linear growth of twice-shocked interfaces are examined across low, moderate and high Atwood number regimes, and further refined based on detailed analyses of their limitations. Furthermore, an analytical model for describing the complete evolution of a twice-shocked interface (DS model) is developed through a comprehensive consideration of the shock-compression, start-up, linear and weakly nonlinear evolution processes. The combination of the refined models and DS model enables, for the first time, an accurate prediction of the complete evolution of interfaces subjected to two co-propagating shock waves. Building upon this, the parameter conditions required to manipulate the RMI with varying Atwood numbers are identified. Verification experiments confirm that suppressing the RMI growth at interfaces with various Atwood numbers via a same-side reshock is feasible and predictable. The present study may shed some light on strategies to suppress hydrodynamic instabilities in inertial confinement fusion through integrated adjustment of material densities and shock timings.

Key words: shock waves

https://doi.org/10.1017/jfm.2025.10828 Published online by Cambridge University Press

© The Author(s), 2025. Published by Cambridge University Press.

1. Introduction

The Richtmyer–Meshkov instability (RMI) arises when a perturbed interface separating two substances of different densities is impulsively accelerated by shock waves. This phenomenon was first theoretically predicted by Richtmyer (1960) and later experimentally confirmed by Meshkov (1969). The RMI has attracted considerable attention over the past several decades (Zhou 2017*a*,*b*, 2024; Zhou *et al.* 2019, 2021) due to its crucial role in numerous significant engineering and scientific applications, particularly in inertial confinement fusion (ICF) (Nuckolls *et al.* 1972; Lindl, McCrory & Campbell 1992; Betti & Hurricane 2016; Zylstra *et al.* 2022; Zhou, Sadler & Hurricane 2025). In ICF, interface perturbations arising from manufacturing imperfections and material inhomogeneities are initially amplified during the early-time shock transit stage by RMI, which in turn seeds the significant growth of the Rayleigh–Taylor instability (Rayleigh 1883; Taylor 1950) occurring in the deceleration phase. These hydrodynamic instabilities can ultimately lead to violent mixing between ablator material and deuterium-tritium fuel, thereby hindering the achievement of high-energy-gain ignition Zhou *et al.* (2025). Presently, extensive research has been conducted on RMI at a once-shocked interface (Zhou 2024), revealing its sensitivity to initial conditions such as perturbation amplitude (Rikanati *et al.* 2003; Wang *et al.* 2023*a*), shock intensity (Holmes *et al.* 1999; Si *et al.* 2025) and Atwood number ($A = (\rho_d - \rho_u)/(\rho_d + \rho_u)$, where ρ_d and ρ_u represent the densities of substances downstream and upstream of the interface, respectively) (Dimonte & Ramaprabhu 2010; Chen *et al.* 2023; Xing *et al.* 2025). Notably, in both conventional direct- and indirect-drive ignition schemes of ICF (Goncharov *et al.* 2003; Lindl *et al.* 2004), as well as in most innovative ignition schemes (Tabak *et al.* 1994; Murakami *et al.* 2006; Betti *et al.* 2007; Zhang *et al.* 2020), a multi-co-propagating-shock drive strategy is commonly employed to achieve the high drive pressure required for ignition while maintaining the target shell at a relatively low entropy. Therefore, investigating the evolution of RMI induced by two co-propagating shock waves (hereafter referred to as 'S-RMI') and exploring strategies to suppress its growth are critical for achieving sustainable fusion energy via ICF.

Under the assumption of incompressibility, which implies that A remains unchanged during the first and second shock–interface interactions, Mikaelian (1985) proposed that a second shock impact from the same side, hereafter referred to as 'same-side reshock', can only promote the instability at a light–heavy interface where $\rho_u < \rho_d$ and $A > 0$. In contrast, at a heavy–light interface where $\rho_u > \rho_d$ and $A < 0$, a same-side reshock can promote, suppress or even freeze the RMI evolution. Additionally, heavy–light interfaces are more commonly encountered than light–heavy interfaces in various types of ICF targets. Therefore, the present study focuses on S-RMI at heavy–light interfaces. Theoretically, Mikaelian (1985) identified thirteen distinct perturbation evolution patterns in an incompressible two-shock system, and proposed a linear superposition model (Mik-L model) to predict the linear evolution of the twice-shocked interface. This model assumes that the post-reshock linear amplitude growth rate is given by the linear superposition of the growth rates induced by the first and second shocks. Notably, according to the pioneering research by Mikaelian (1994) on the influence of compressibility on RMI, the possibility analysis based on the incompressibility assumption is inadequate for describing S-RMI in compressible flows (see Appendix B for details). Numerically, Charakhch'yan (2000) investigated S-RMI at the free surface of liquid aluminium, with pre-first-shock Atwood number A_0 (or post-first-shock Atwood number A_1) of -1.0. An empirical model (Cha-L model) was proposed to predict the linear amplitude growth rate of the twice-shocked free surface, and the conditions for achieving the 'freeze-out' phenomenon were

https://doi.org/10.1017/jfm.2025.10828 Published online by Cambridge University Press

derived. Subsequently, Charakhch'yan (2001) confirmed via numerical simulations that the Cha-L model also applies to describe the post-reshock linear evolution of gaseous interfaces (air–He and freon–air interfaces, with A_1 values -0.76 and -0.55, respectively) under typical shock-tube experimental conditions. Karkhanis *et al.* (2017) numerically investigated the ejecta phenomenon on a metal free surface impulsively accelerated by two co-propagating shock waves, with A_0 (A_1) values -1.0, which can be treated as a limiting case of S-RMI. It was demonstrated that a model proposed for the ejecta phenomenon induced by a single shock (Cherne *et al.* 2015) can also reasonably predict the reshock-induced ejecta production.

Experimentally, Merritt *et al.* (2023) utilised a hybrid direct–indirect laser drive scheme to generate two co-propagating shock waves, and investigated the S-RMI occurring at the interface separating iodine-doped CH plastic from low-density CH or SiO_2, with A_0 values -0.87. Moreover, by employing a specially designed stepped flyer, composed of alternating heavy and light materials, to impact a PMMA target and thereby generate two co-propagating shocks, Schill *et al.* (2024) investigated the S-RMI at the free surface of the target, with A_0 (A_1) values -1.0. Based on the linear superposition principle (Mikaelian 1985), both Merritt *et al.* (2023) and Schill *et al.* (2024) demonstrated the suppression of the RMI growth through a same-side reshock. However, the perturbation evolution in these experiments would be influenced by waves other than two primary shocks, as well as complex physical and chemical processes such as material phase transition and plasma diffusion, making it challenging to conduct a detailed investigation of the mechanisms underlying S-RMI. Recently, Wang *et al.* (2022) developed a shock-tube facility capable of generating two co-propagating shocks with controllable intensities and time intervals while offering a 'clean' experimental environment, providing a reliable platform for the experimental investigation of S-RMI. Subsequently, Zhai *et al.* (2025) proposed combined models to describe the complete evolution of a once-shocked interface and the linear growth of a twice-shocked interface, and systematically discussed the possible amplitude evolution patterns building upon the work of Mikaelian (1985). Using the specific shock-tube facility, the S-RMI at an SF_6–air interface ($A_1 = -0.68$) was experimentally investigated. Their models were validated for application to S-RMI at an SF_6–air interface, and all seven possibilities for instability manipulation were achieved in experiments.

Overall, previous studies on S-RMI are limited to scenarios where A is either constant or varies within a narrow range. However, in ICF, the materials composing different layers of various targets are diverse (Lindl *et al.* 2014; Kritcher *et al.* 2022), leading to significant variations in A of relevant interfaces. The evolution mechanisms and suppression strategies of S-RMI under varying A conditions remain unclear. Furthermore, existing models have not been evaluated under diverse A conditions, and cannot describe the complete evolution of twice-shocked interfaces. These gaps motivate the present work. In this study, we first assess and analyse the applicability of existing models in predicting the evolution of once-shocked interfaces and the post-reshock linear amplitude growth under diverse A conditions. On this basis, analytical models for predicting the complete evolution of S-RMI with various A are developed and evaluated. With the experimentally obtained one-dimensional (1-D) flow parameters and the analytical models, the theoretical parameter conditions for suppressing the RMI growth are derived. Finally, shock-tube experiments are conducted to evaluate the feasibility and predictability of suppressing the RMI growth via a same-side reshock under varying A conditions.

https://doi.org/10.1017/jfm.2025.10828 Published online by Cambridge University Press

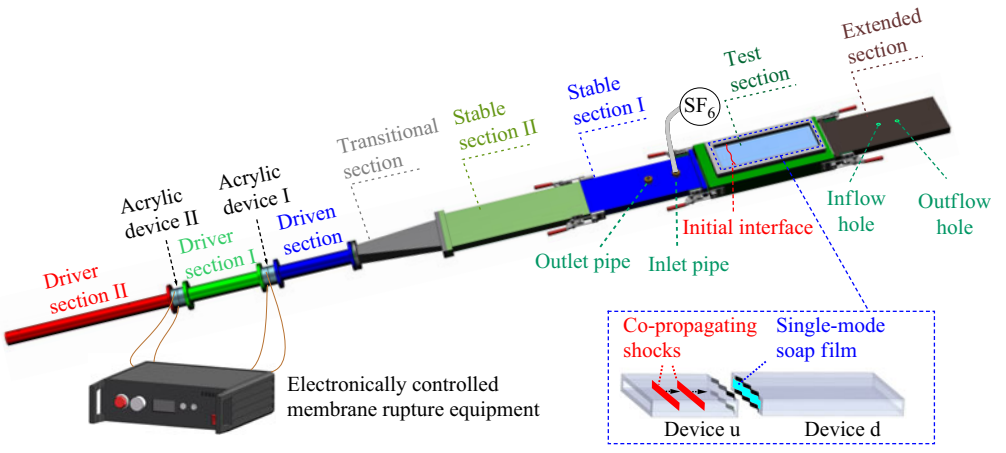


Figure 1. Sketch of the shock-tube facility for generating two co-propagating shock waves, and the interface formation devices.

2. Experimental methods and 1-D flow parameter determination

2.1. *Experimental methods*

The evolution of the once-shocked and twice-shocked interfaces is highly sensitive to the flow conditions (Zhou 2024; Cao *et al.* 2024). Therefore, conducting a desirable experimental investigation on the evolution mechanisms and manipulation approaches of S-RMI requires reliable methods for the controlled generation of shock waves and interfaces. In this study, experiments are conducted using a newly developed shock-tube facility (Wang *et al.* 2022), as illustrated in figure 1. Its capability of generating two co-propagating shocks with controllable time intervals (Δt) and intensities has been demonstrated and validated in previous studies (Wang *et al.* 2022; Cao *et al.* 2024), with further details available therein. The first shock is generated at the junction of the driven section and driver section I, with the sections containing air at pressures 101.3 and 304.0 kPa, respectively. The polyester membrane separating these two sections has thickness 12.5 μm. The second shock is generated at the junction of driver sections I and II separated by a polyester membrane having thickness 25 μm, with driver section II filled with air at pressure 608.0 kPa.

The soap-film technique, which has been extensively utilised and validated in prior studies (Wang *et al.* 2022; Chen *et al.* 2023), is employed to generate the initial interface. The transparent interface formation devices (devices u and d), as illustrated in figure 1, are constructed by assembling two acrylic plates with pedestals. The internal cross-sectional dimensions of devices u and d, as well as those of the other rectangular sections of the shock tube, are 140 mm × 6 mm. To realise a wide-range variation in A, air on both sides of the soap film should be replaced with different gases. Therefore, in comparison with the original facility reported by Wang *et al.* (2022), an additional stable section (stable section I) is incorporated to facilitate gas replacement upstream of the soap film. Additionally, to prolong the effective duration of the experiment, an extended section is added downstream of the test section to delay the influence of reflected waves on the evolving interface. The variation in A is achieved by employing different downstream gases (Kr, air or He) while maintaining the main component of the upstream gas (SF_6) unchanged. The procedures for gas replacement are as follows. First, a flat polyethylene acetate diaphragm and a polyester film are affixed to the left-hand side of stable section I and the right-hand side of the extended section, respectively. Subsequently, after forming a single-mode soap film on the

https://doi.org/10.1017/jfm.2025.10828 Published online by Cambridge University Press

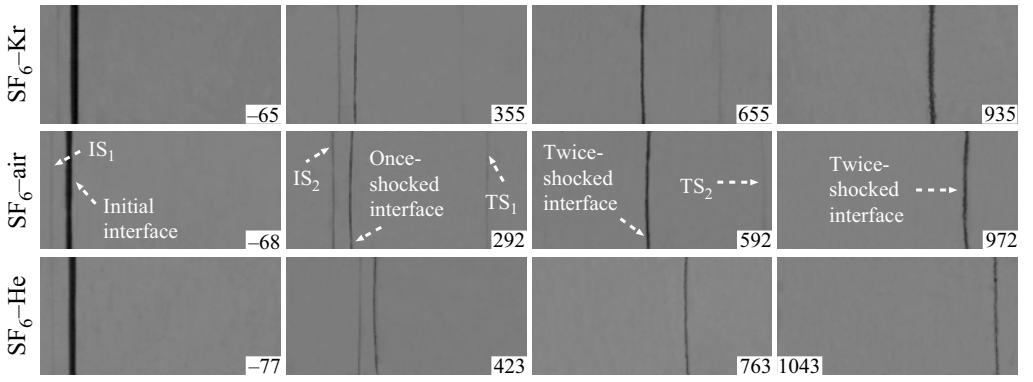


Figure 2. Experimental schlieren photographs of the interactions between two co-propagating shocks and unperturbed interfaces with different gas combinations (SF_6–Kr, SF_6–air and SF_6–He). Numbers represent time in μs.

left-hand side of device d, devices u and d are carefully assembled and inserted into the test section. Thereafter, SF_6 is slowly injected into stable section I and device u through the inlet pipe, while air is released through the outlet pipe. Meanwhile, except for the experiments with an SF_6–air interface, the light gas (Kr or He) is injected into device d and the extended section through the inflow hole, while air is discharged via the outflow hole. As a result, a single-mode heavy–light interface is formed. Notably, the rate and duration of gas injection are kept constant to ensure similar gas fractions across different runs with the same gas combination.

The flow evolution is captured using a high-speed schlieren imaging system. The high-speed video camera (FASTCAM SA-Z, Photron Limited) operates at frame rate 50 000 frames per second, with exposure time 0.347 μs. The spatial resolution of the schlieren images is approximately 0.27 mm pixel^{-1}. The ambient pressure and temperature are 101.3 ± 0.1 kPa and 298.5 ± 1.0 K, respectively.

2.2. *Method evaluation and 1-D flow parameter determination*

To evaluate the experimental methods and determine the general 1-D flow parameters in scenarios with various A, experiments on the interactions between two co-propagating shocks and unperturbed interfaces with different gas combinations (SF_6–Kr, SF_6–air and SF_6–He) are conducted. For each gas combination, three experimental runs are conducted following an identical procedure, resulting in flow fields with reproducible characteristics and consistent 1-D parameters, as detailed in Appendix A. For clarity, only one run for each gas combination is presented for detailed discussion below.

Experimental schlieren images of the evolution of initial planar heavy–light interfaces with different gas combinations accelerated by two co-propagating shock waves are presented in figure 2. The experiment with an SF_6–air interface is taken as an example to illustrate the detailed flow evolution process. The temporal origin ($t = 0$ μs) is defined as the instant at which the first shock (IS_1) hits the initial interface. When IS_1 impacts the initial interface, a transmitted shock wave (TS_1) and reflected rarefaction waves (RW_1) are generated. Simultaneously, the once-shocked interface begins to move and evolve. The second shock (IS_2) enters the observation domain at approximately 292 μs. When reshock occurs, the second transmitted shock (TS_2) and reflected rarefaction waves (RW_2) are generated. As observed from the schlieren images, the width of the twice-shocked interface exhibits a progressive increase during the evolution process (592–972 μs). This

https://doi.org/10.1017/jfm.2025.10828 Published online by Cambridge University Press

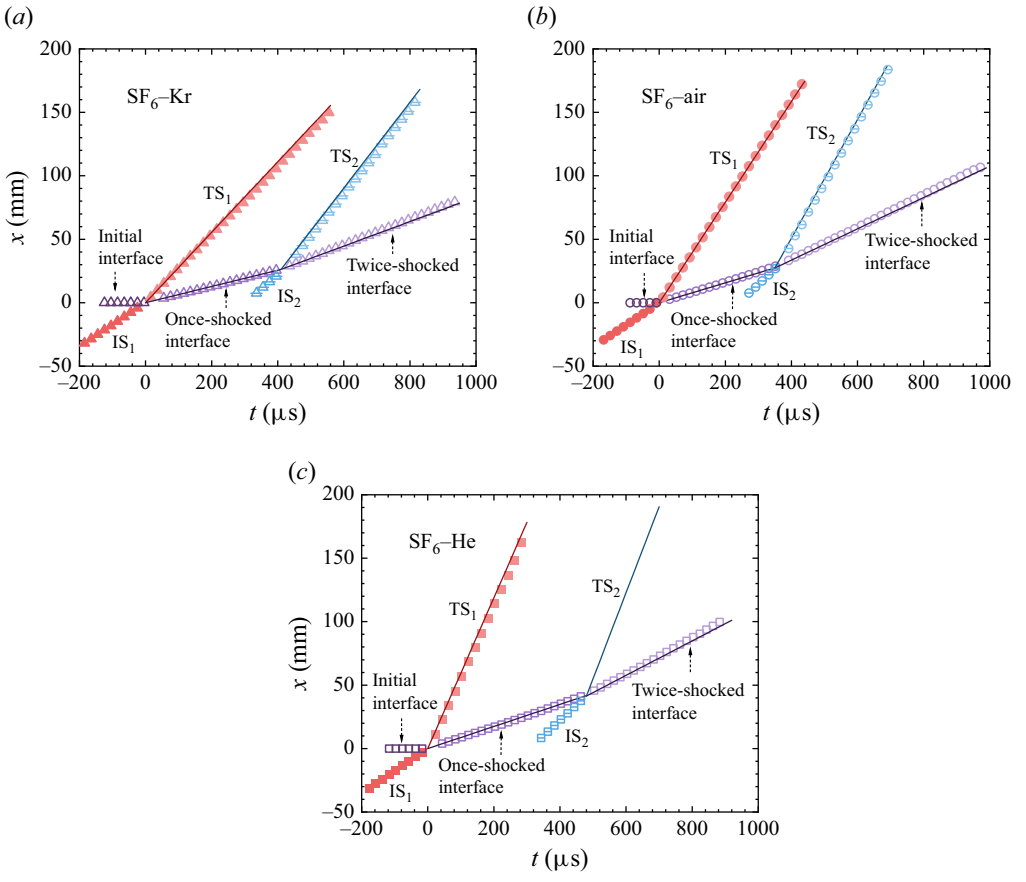


Figure 3. Trajectories of interface and waves for experiments with different gas combinations. Symbols and lines indicate experimental and theoretical results, respectively. Notably, the absence of data for TS_2 in the experiment with an SF_6–He interface is due to its relatively low strength, combined with the low density of He, which makes it almost invisible in the schlieren photographs.

phenomenon is primarily attributed to the gradual detachment of broken soap-film droplets from the interface, resulting in a relatively significant density gradient in the flow field adjacent to the interface. All shock waves are essentially planar, and the twice-shocked interface maintains an approximately planar configuration before exiting the observation region (972 μs).

The gas components on both sides of the initial interface, as well as the pre- and post-reshock flow parameters, are determined based on the 1-D gas dynamics theory. The experimentally measured velocity of IS_1 (v_1^{is}) is adopted as an initial condition. By matching the experimentally measured velocities of TS_1 and the once-shocked interface (v_1^{ts} and Δu_1, respectively) with their theoretical counterparts, the gas components on both sides of the initial interface and the post-first-shock flow parameters are determined. Further, using the experimentally measured velocity of IS_2 (v_2^{is}) as another initial condition, the post-reshock flow parameters are determined. The trajectories of shock waves and interfaces, extracted from experiments and predicted based on the 1-D flow parameters, are presented in figure 3, where $x = 0$ denotes the location of the initial interface. The theoretical predictions agree well with the experimental data, thereby confirming the reliability and accuracy of the determined 1-D flow parameters. The key

https://doi.org/10.1017/jfm.2025.10828 Published online by Cambridge University Press

https://doi.org/10.1017/jfm.2025.10828 Published online by Cambridge University Press

Gas combination	Gas u	Gas d	A_0	v_1^{is}	M_1	v_1^{ts}	E-v_1^{ts}	Δu_1	E-Δu_1	A_1	v_2^{is}	M_2	v_2^{ts}	E-v_2^{ts}	Δu_2	E-Δu_2	A_2
SF_6–Kr	93 %SF_6 + 7 %air	80 %Kr + 20 %air	−0.31	175.15	1.25	277.60	0.10 %	64.03	−0.48 %	−0.36	223.73	1.11	337.58	0.50 %	32.55	−4.49 %	−0.39
SF_6–air	93 %SF_6 + 7 %air	100 %air	−0.65	175.08	1.24	396.56	0.15 %	77.78	0.31 %	−0.67	239.73	1.13	468.63	−0.60 %	45.60	−3.16 %	−0.68
SF_6–He	93 %SF_6 + 7 %air	63 %He + 37 %air	−0.82	175.15	1.25	594.10	0.22 %	86.97	0.01 %	−0.83	247.57	1.13	678.24	—	48.74	−2.28 %	−0.84

Table 1. General 1-D flow parameters for experiments with different gas combinations: gases u and d are gases upstream and downstream of the interface, respectively; A_0, A_1 and A_2 are pre-first-shock, post-first-shock and post-reshock Atwood numbers, respectively; v_1^{is} and v_1^{ts} (v_2^{is} and v_2^{ts}) are velocities of IS_1 and TS_1 (IS_2 and TS_2), respectively; E-v_1^{ts} (E-v_2^{ts}) are relative deviations between experimental v_1^{ts} (v_2^{ts}) and its theoretical counterpart; M_1 and M_2 are Mach numbers of IS_1 and IS_2 when impacting the interface, respectively; Δu_1 and Δu_2 are jump velocities of interface induced by IS_1 and IS_2, respectively; E-Δu_1 (E-Δu_2) are relative deviations between experimental Δu_1 (Δu_2) and its theoretical counterpart. Unit of all parameters representing velocity is m s^{-1}.

flow parameters for experiments with various gas combinations are summarised in table 1. Given the favourable experimental repeatability as detailed in Appendix A, the 1-D flow parameters presented in table 1 are regarded as those of subsequent experiments with the same gas combination.

Knowing the 1-D flow parameters, the procedure for determining Δt is as follows. First, the positions of IS_1 and the initial interface in the photograph immediately preceding the first impact are extracted. Then, based on these data and v_1^{is}, the corresponding time of the photograph immediately preceding the first impact can be determined. Since the temporal resolution of schlieren photographs is constant, the time corresponding to each photograph is obtained. Subsequently, the positions of IS_2 and the once-shocked interface in the photograph immediately preceding the reshock are extracted. Based on their positions and known velocities, the precise moment of reshock can be calculated, thus realising the determination of Δt.

Given the extended length of the facility in the streamwise direction and the low height of the experimental flow field (6 mm), it is necessary to assess the boundary-layer effects on interface evolution. According to our understanding, the influence of the boundary layer on the instability can be attributed primarily to two mechanisms. First, the rarefaction waves generated by the boundary layer decelerate the interface, depositing additional vorticity and thereby affecting the instability evolution. Second, the boundary layer at the interface introduces three-dimensional effects, which in turn affect the evolution of perturbations on the interface.

The influence of the rarefaction waves is evaluated by comparing experimental interface/shock velocities with 1-D theoretical predictions that do not consider these waves. The relative deviations between the experimental and theoretical interface/transmitted shock velocities (defined as $E\text{-}f = (v^t - v^e)/v^t$, where v^t and v^e represent theoretical and experimental f, respectively), as illustrated in table 1, are all below 4.5 %. This favourable agreement indicates that the rarefaction waves have a minimal influence on the motion of the interface and shocks during the experimental observation period, and thus exert a negligible effect on the instability evolution.

The influence of the boundary layer at the interface is assessed via the boundary-layer displacement thickness. Since the intensities of IS_1 and IS_2 are weak (with Mach numbers below 1.30, as shown in table 1), the flow field behind them can be reasonably considered laminar and incompressible. Thus the following formula proposed by Mirels (1956) is employed to estimate the boundary-layer displacement thickness at the twice-shocked interface:

$$\delta_2 = \sqrt{\frac{\pi \mu_2 x_d}{\rho_2 \left(v_2^{ts} - \Delta u_1 - \Delta u_2\right)}} \left(\frac{v_2^{ts}}{v_2^{ts} - \Delta u_1 - \Delta u_2} - 1 \right), \tag{2.1}$$

where μ_2 and ρ_2 represent the viscosity coefficient and density of post-reshock gases, respectively; x_d corresponds to the maximum distance between the twice-shocked interface and TS_2 during the experiment; v_2^{ts} and Δu_2 denote the velocity of TS_2 and the interface jump velocity induced by IS_2, respectively. The relevant parameters and predictions for δ_2 upstream and downstream of the interface (δ_2^u and δ_2^d) are summarised in table 2. It is evident that in all scenarios, the values of δ_2^u and δ_2^d are significantly smaller than the height of the experimental flow field. This indicates that the interface exhibits limited three-dimensional features, suggesting that the boundary layer at the interface has a negligible influence on the perturbation evolution.

https://doi.org/10.1017/jfm.2025.10828 Published online by Cambridge University Press

Gas combination	μ_2^u	μ_2^d	ρ_2^u	ρ_2^d	x_d	δ_2^u	δ_2^d
SF_6–Kr	1.65×10^{-5}	2.23×10^{-5}	9.91	4.39	151.03	0.02	0.04
SF_6–air	1.55×10^{-5}	2.08×10^{-5}	8.68	1.66	160.53	0.02	0.05
SF_6–He	1.52×10^{-5}	1.98×10^{-5}	7.92	0.69	272.03	0.01	0.05

Table 2. Boundary-layer displacement thickness at the twice-shocked interface (δ_2) and relevant parameters: μ_2^u and μ_2^d (ρ_2^u and ρ_2^d) are viscosity coefficients (densities) of post-reshock gases u and d, respectively; x_d is the maximum distance between the twice-shocked interface and TS_2 during the experiment; δ_2^u and δ_2^d are δ_2 upstream and downstream of the interface, respectively. Units of parameters representing viscosity coefficient, density and distance are Pa s, kg m^{-3} and mm, respectively.

3. Evolution law of S-RMI under diverse Atwood number conditions

For a once-shocked interface with scaled initial amplitude ($|ka_0|$, where k represents the perturbation wavenumber, and a_0 denotes the initial amplitude which is presumed to be negative) satisfying the small-amplitude criterion ($|ka| \ll 1$), previous research Zhou (2017*a*,*b*, 2024) suggests that its evolution can be broadly divided into six successive stages: shock-compression stage (perturbation amplitude, denoted as $|a_1|$, decreases under compression), start-up stage (amplitude growth rate, denoted as $\dot{a}_1$, increases gradually), linear stage ($\dot{a}_1$ maintains nearly constant), weakly nonlinear stage ($\dot{a}_1$ decreases, with bubble and spike structures gradually becoming prominent), strongly nonlinear stage (roll-up structures emerge), and turbulent mixing stage (multiscale vortices appear and intense mixing of substances occurs). Notably, once the interface evolution enters the strongly nonlinear stage, the mixing of substances on two sides of the interface begins. This highlights the importance of suppressing the instability prior to the onset of the strongly nonlinear regime in practical applications. Therefore, the present study focuses on scenarios where the pre-reshock interface has not yet entered the strongly nonlinear regime.

The evolution state of the pre-reshock interface, which is determined by Δt for given shocks and initial interface, would significantly affect the post-reshock flow evolution (Karkhanis & Ramaprabhu 2019; Cao *et al.* 2024). Specifically, if reshock occurs before the phase inversion (i.e. a process during which the absolute perturbation amplitude gradually decreases to zero) is completed, the vorticity deposited by IS_2 has the same sign as that deposited by IS_1. Moreover, the vorticity deposition decreases with increasing Δt, due to the diminished interface amplitude during the phase-inversion process. Conversely, if reshock occurs after the phase inversion is completed, the vorticity deposited by IS_2 has the opposite sign to that deposited by IS_1, and a larger amount of vorticity is deposited for longer Δt, due to the larger pre-reshock amplitude. Therefore, to better understand the evolution law of S-RMI under diverse A conditions, two experimental runs with the same initial perturbation but varying Δt are conducted for each gas combination (SF_6–Kr, SF_6–air and SF_6–He). The perturbation wavelength λ and $|ka_0|$ are fixed at 40 mm and 0.19, respectively, and the experiments are labelled by the combination of $|A_1|$ and Δt.

3.1. *Flow features and interface morphology*

Schlieren images of experiments with different A_1 and Δt are presented in figure 4. In all six experiments, the pre-reshock interface remains in the linear or weakly

https://doi.org/10.1017/jfm.2025.10828 Published online by Cambridge University Press

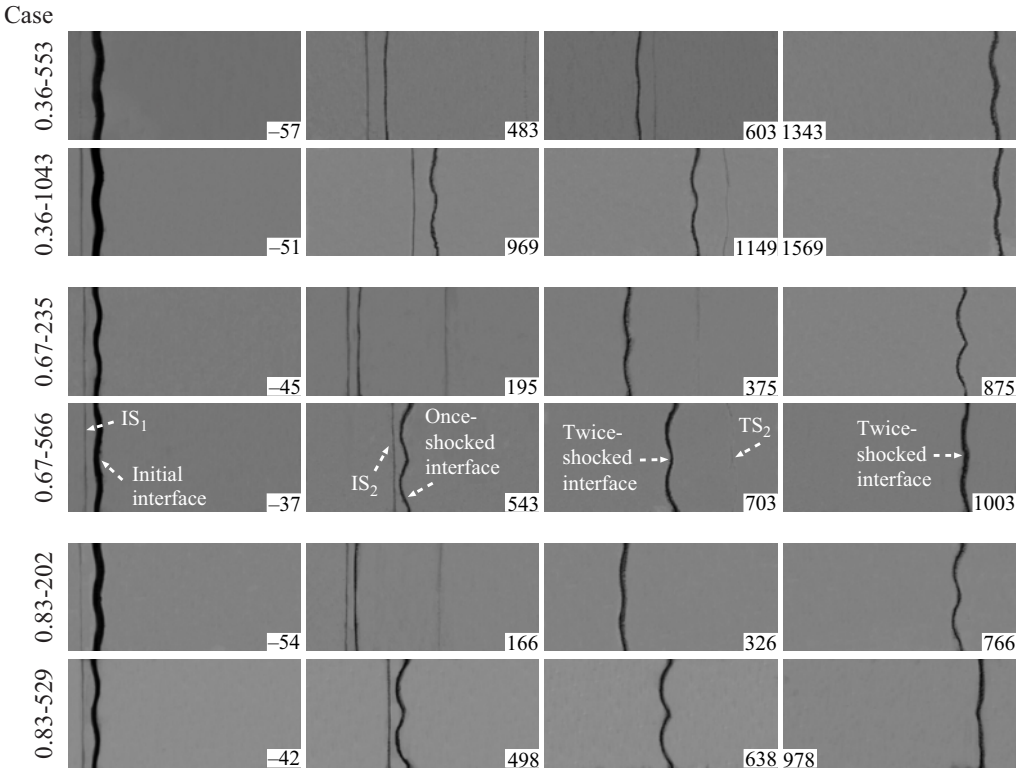


Figure 4. Schlieren photographs of experimental cases with various A_1 and Δt.

nonlinear regime, meeting the research needs. Case 0.67-566 is selected to exemplify the general interface evolution process. The interface amplitude decreases after the first shock impact, and the phase-inversion process is completed prior to the arrival of IS_2 (543 μs). Following the reshock, the interface amplitude decreases gradually (543–1003 μs). In cases with relatively short Δt (i.e. cases 0.36-553, 0.67-235 and 0.83-202), the interface has just completed the phase-inversion process when IS_2 arrives, with amplitude remaining small. After the reshock, the interface amplitude continues to grow. In contrast, for cases with relatively long Δt (i.e. cases 0.36-1043, 0.67-566 and 0.83-529), the interface amplitude has increased to a considerable level prior to the reshock, and the interface undergoes a second phase-inversion process after the reshock. Additionally, in cases with higher $|A_1|$, the interface evolves at an overall faster rate in both the pre- and post-reshock phases. These observations qualitatively indicate that both A_1 and Δt affect the evolution state of the pre-reshock interface, which subsequently influences the post-reshock evolution. In the following, quantitative analyses on the amplitude evolution of the once-shocked and twice-shocked interfaces are performed.

3.2. *Once-shocked interface*

To predict the complete amplitude evolution of a once-shocked heavy–light interface, Zhai *et al.* (2025) proposed a combined model (FS model) that comprehensively considers the shock-compression, start-up, linear and weakly nonlinear evolution stages. The construction of the FS model is detailed as follows. To facilitate understanding, the flow

https://doi.org/10.1017/jfm.2025.10828 Published online by Cambridge University Press

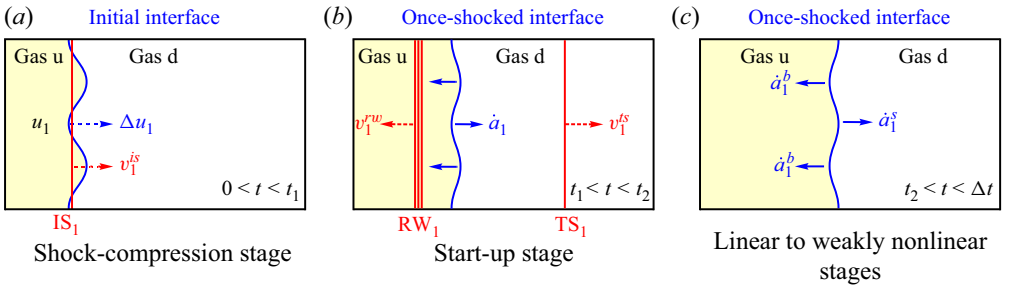


Figure 5. Flow features (including wave patterns and interface deformation) and associated key physical parameters at various stages of the once-shocked interface evolution.

features (including wave patterns and interface deformation) at various stages of the once-shocked interface evolution, along with the key physical parameters associated with the FS model, are illustrated in figure 5.

3.2.1. *Shock-compression stage*

Following the impact of IS_1 on the initial interface at $t = 0$, $|a_1|$ decreases continuously until the completion of the shock–interface interaction (Richtmyer 1960). The expressions for the duration of the interaction (t_1) and the amplitude variation during this stage were proposed by Richtmyer (1960), and can be written as

$$t_1 = 2\,|a_0|/v_1^{is}, \tag{3.1}$$

$$a_1(t) = a_0 + \Delta u_1\, t/2. \tag{3.2}$$

These relations, collectively referred to as the R model hereafter, have been extensively validated (Zhou 2024), and were incorporated into the FS model.

3.2.2. *Start-up stage*

During this stage, $\dot{a}_1(t)$ rises from zero and gradually reaches an asymptotic value $\dot{a}_1^+$ under the drive of pressure perturbation (Yang, Zhang & Sharp 1994). Lombardini & Pullin (2009) proposed an analytical model to forecast the characteristic time of the start-up process for a once-shocked light–heavy interface. For a once-shocked heavy–light interface, Yang *et al.* (1994) deduced a compressible linear theory to predict the perturbation evolution in the start-up period. However, this theory needs to be solved numerically. Recently, following the approach of Lombardini & Pullin (2009), Li *et al.* (2024) deduced an analytical solution for predicting the duration of the start-up process for a once-shocked heavy–light interface, which can be expressed as

$$t_2 - t_1 = \frac{1}{k}\left(\frac{1 - A_1}{v_1^{rw} + \Delta u_1} + \frac{1 + A_1}{v_1^{ts} - \Delta u_1}\right). \tag{3.3}$$

Here, t_2 denotes the end moment of the start-up period, while v_1^{rw} represents the velocity of RW_1. In addition, Li *et al.* (2024) proposed that the amplitude growth in the start-up stage can be described as

$$\dot{a}_1(t) = \frac{2\dot{a}_1^+}{(1 + A_1)\coth\left(kL_1^{ts}\right) + (1 - A_1)\coth\left(kL_1^{rw}\right)} \quad (t_1 < t < t_2), \tag{3.4}$$

https://doi.org/10.1017/jfm.2025.10828 Published online by Cambridge University Press

where

$$\begin{cases} L_1^{ts} = \left(v_1^{ts} - \Delta u_1\right)(t - t_1), \\ L_1^{rw} = \left(v_1^{rw} + \Delta u_1\right)(t - t_1), \end{cases} \tag{3.5}$$

are the displacements of TS_1 and RW_1, respectively.

3.2.3. *Linear stage*

When $t > t_2$, the amplitude evolution is commonly regarded as entering the linear stage, during which $\dot{a}_1(t)$ remains nearly constant at $\dot{a}_1^+$. However, the linear stage is an approximate description of a period where nonlinearity exists but remains limited, and defining the demarcation point between the linear and nonlinear stages is challenging. Therefore, the FS model considers the end of the start-up period as the beginning of both the linear and nonlinear stages. In other words, the linear stage is considered to be of negligible duration in the FS model. The irrotational WN model (WNi model) (Wouchuk & Nishihara 1997; Wouchuk 2001), validated for scenarios where the shock intensity (defined as $1 - p_{in}/p_{be}$, where p_{in} and p_{be} represent the pressures of fluids in front of and behind the shock, respectively) is lower than 0.5 (Li *et al.* 2024), was adopted to predict $\dot{a}_1^+$. The WNi model can be written as

$$\dot{a}_1^+ = ka_0 \left[\frac{1 - A_1}{2} \left(1 + \frac{v_1^{rw}}{v_1^{is}} \right) (u_1 - \Delta u_1) + \Delta u_1 \frac{1 + A_1}{2} \left(1 - \frac{v_1^{ts}}{v_1^{is}} \right) \right], \tag{3.6}$$

where u_1 represents the velocity of the fluid behind IS_1. The system (3.3)–(3.6), collectively referred to as the Li model, was incorporated into the FS model.

3.2.4. *Weakly nonlinear stage*

As high-order harmonics emerge and become significant, $\dot{a}_1(t)$ decreases progressively, signifying that the interface evolution has entered the weakly nonlinear stage (Zhou 2024). Zhai *et al.* (2025) experimentally demonstrated that the DR model (Dimonte & Ramaprabhu 2010) accurately describes the weakly nonlinear evolution of a once-shocked SF_6–air interface, and therefore adopted it to construct the FS model. The DR model can be expressed as

$$\begin{cases} \dot{a}_1(t) = \left[\dot{a}_1^b(t) + \dot{a}_1^s(t)\right]/2, \\ \dot{a}_1^{b/s}(t) = \dot{a}_1^+ \dfrac{1 + k\dot{a}_1^+(t - t_2)(1 \mp |A_1|)}{1 + E^{b/s}k\dot{a}_1^+(t - t_2) + (1 \mp |A_1|)F^{b/s}k^2\dot{a}_1^{+2}(t - t_2)^2}, \end{cases} \tag{3.7}$$

where superscripts b and s represent bubble and spike, respectively, $E^{b/s} = [4.5 \pm |A_1| + (2 \mp |A_1|)(1 - \Delta u_1/v_1^{is})k|a_0|]/4$ and $F^{b/s} = 1 \pm |A_1|$.

The comparison between the present experimental results and corresponding theoretical predictions by the FS model, composed of (3.1)–(3.7), is illustrated in figure 6. It can be observed that the FS model provides reasonable predictions for the entire amplitude evolution process under low and moderate $|A_1|$ conditions, as well as for the evolution of the SF_6–He interface from the shock-compression to linear stages. However, this model fails to accurately predict the weakly nonlinear evolution of the SF_6–He interface. Notably, the R and Li models have been demonstrated to be valid over a wide range of A_1 conditions (Xing *et al.* 2025). Therefore, the failure of the FS model should be attributed to the limitation of the DR model. In our previous work (Xing *et al.* 2025), an empirical nonlinear model (mSEA model) was proposed based on existing models and extensive experimental

https://doi.org/10.1017/jfm.2025.10828 Published online by Cambridge University Press

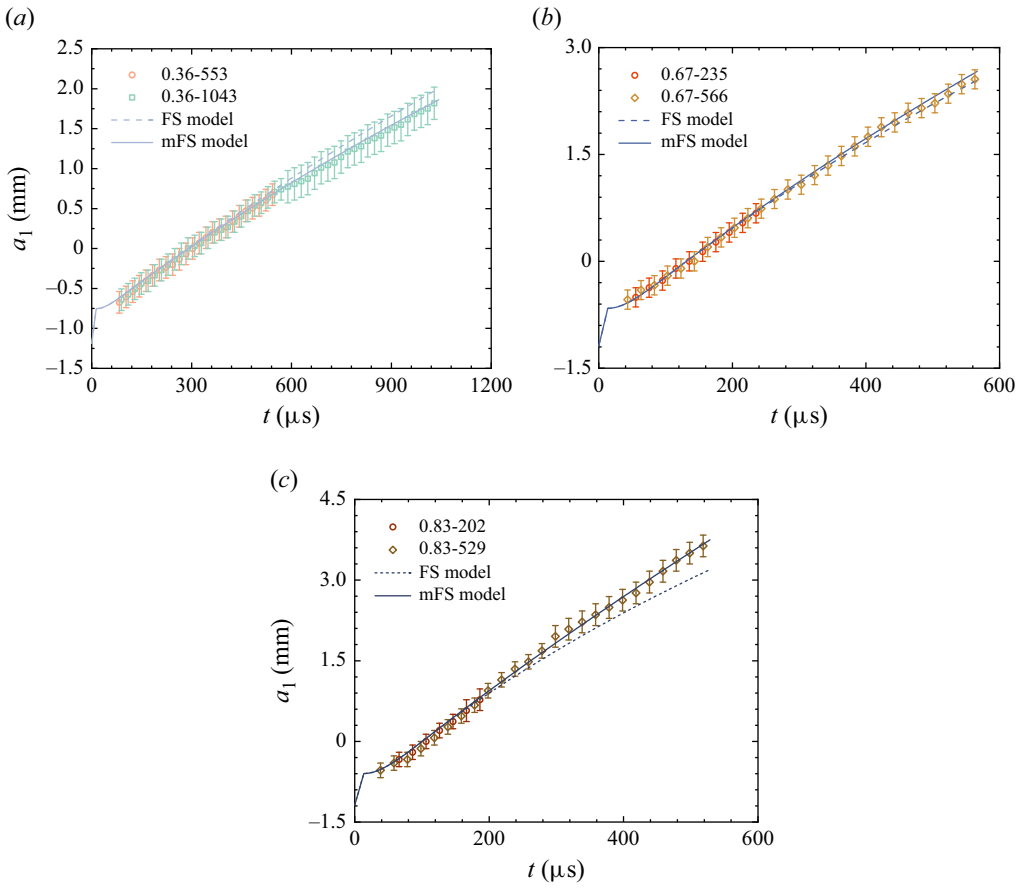


Figure 6. Overall amplitude evolutions of once-shocked heavy–light interfaces with various A_1. Symbols denote experimental results; dashed and solid lines represent theoretical predictions by the FS and mFS models, respectively. Error bars represent potential errors in extracting the interface amplitude, with a length equal to half the width of the interface in the experimental schlieren image, and the same hereafter.

results (Chen *et al.* 2023; Xing *et al.* 2025), which can be described as

$$\begin{cases} \dot{a}_1(t) = \left[\dot{a}_1^b(t) + \dot{a}_1^s(t)\right]/2, \\ \dot{a}_1^{b/s}(t) = \dot{a}_1^+ \dfrac{1 + k\dot{a}_1^+(t - t_2)}{1 + (2 \mp |A_1|)(1.07 \pm |A_1|)k\dot{a}_1^+(t - t_2) + \dfrac{1 \pm |A_1|}{1 + |A_1|}\dfrac{1}{2\pi C_1}k^2\dot{a}_1^{+2}(t - t_2)^2}, \end{cases} \tag{3.8}$$

where C_1 is given by $1/3\pi$ for cases with $|A_1| \geqslant 0.5$, and $1/2\pi$ for cases where $|A_1| \to 0$. The mSEA model has been shown to effectively describe the weakly nonlinear evolution across the ranges of A_1 from -0.95 to -0.35, and from 0.30 to 0.86. Therefore, we can obtain a modified FS model (mFS model) by substituting the DR model with the mSEA model. The overall amplitude evolution predicted using the mFS model is presented in figure 6. The close agreement between the mFS model predictions and experimental results suggests that the mFS model is capable of reliably predicting the complete amplitude evolution of once-shocked heavy–light interfaces with various A_1.

https://doi.org/10.1017/jfm.2025.10828 Published online by Cambridge University Press

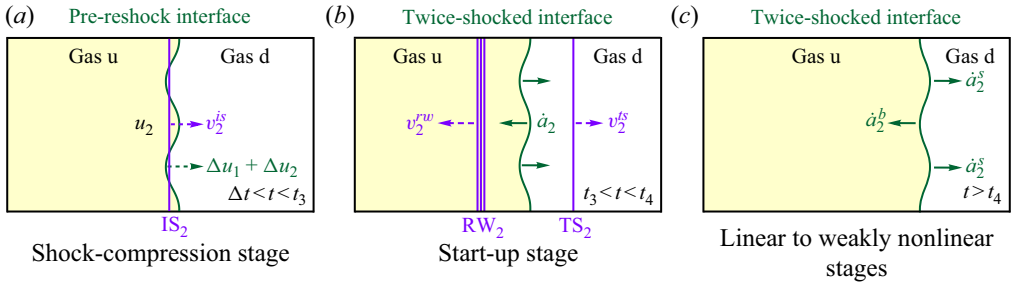


Figure 7. Flow features and associated key physical parameters at diverse stages following reshock. The flow depicted represents a typical case in which the reshock occurs after the phase inversion of the once-shocked interface, and the twice-shocked interface subsequently undergoes a second phase inversion.

3.3. *Twice-shocked interface*

Given the complex characteristics of the pre- and post-reshock flow fields, two simplifying assumptions are made in developing the models for the twice-shocked interface evolution. First, the influence of the rippled RW_1 on IS_2 is negligible, i.e. IS_2 can be treated as a planar shock. Second, the non-uniformities in the flow field behind TS_1 have a negligible influence on TS_2, i.e. the flow field ahead of TS_2 can be approximated as uniform. An evaluation of these two assumptions is provided in Appendix C. Moreover, to aid comprehension of the model construction, the flow features and associated key physical parameters at diverse stages following the reshock are sketched in figure 7. Notably, multiple scenarios may arise depending on the pre-reshock interface configuration and the subsequent post-reshock evolution. The flow depicted in figure 7 represents a typical case in which the reshock occurs after the phase inversion of the once-shocked interface, and the twice-shocked interface subsequently undergoes a second phase inversion.

3.3.1. *Linear amplitude growth*

To describe the linear evolution following reshock, Mikaelian (1985) proposed a linear superposition principle, which assumes that the post-reshock linear amplitude growth rate ($\dot{a}_2^+$) is equal to the linear superposition of the pre-reshock amplitude growth rate ($\dot{a}_2^-$) and the additional growth rate induced by reshock ($\Delta\dot{a}$). This principle has since served as a theoretical basis for numerous investigations. Specifically, the Mik-L model proposed by Mikaelian (1985) assumes that $\dot{a}_2^+$ equals the sum of $\dot{a}_2^-$ and $\Delta\dot{a}$ calculated using the impulsive model. As a result, the Mik-L model is applicable only for scenarios with a light–heavy interface, and is expected to fail when reshock occurs at the nonlinear evolution stage of the once-shocked interface. Building upon the linear superposition principle, Charakhch'yan (2000, 2001) proposed the Cha-L model for predicting $\dot{a}_2^+$. However, the Cha-L model does not include a relation/model to predict the amplitude evolution of the once-shocked interface, and instead relies on $\dot{a}_2^-$ extracted from numerical simulations or experiments. Thus its application is significantly constrained. Additionally, the Cha-L model is expected to be applicable only when reshock occurs at strongly nonlinear stages, as it assumes that $\Delta\dot{a}$ is independent of the pre-reshock perturbation characteristics. To address the limitations of the previous models, Zhai *et al.* (2025) proposed a new model (LS model) to predict $\dot{a}_2^+$ of an SF_6–air interface subjected to reshock occurring at any stage prior to the onset of strong nonlinearity. The LS model can

https://doi.org/10.1017/jfm.2025.10828 Published online by Cambridge University Press

Case	$\dot{a}^+_{2,e}$ (m s^{-1})	$\dot{a}^+_{2,ls}$ (m s^{-1})	$ka^-_{2,mfs}$	$\dot{a}^-_{2,mfs}$ (m s^{-1})	$\dot{a}^+_{2,mls}$ (m s^{-1})
0.36-553	1.37 ± 0.05	1.43	0.11	2.56	1.35
0.36-1043	-0.94 ± 0.03	-1.10	0.29	2.20	-0.90
0.67-235	3.37 ± 0.12	3.39	0.11	6.52	3.55
0.67-566	-5.04 ± 0.24	-5.86	0.42	5.42	-5.16
0.83-202	3.85 ± 0.19	3.27	0.15	9.17	3.91
0.83-529	-10.10 ± 0.36	-11.83	0.59	8.02	-10.65

Table 3. Experimental and theoretical results related to the post-reshock linear amplitude evolution: $\dot{a}^+_{2,e}$, $\dot{a}^+_{2,ls}$ and $\dot{a}^+_{2,mls}$ are post-reshock linear amplitude growth rates obtained from experiments and predicted by the LS and mLS models, respectively; $ka^-_{2,mfs}$ and $\dot{a}^-_{2,mfs}$ are pre-reshock dimensionless amplitude and amplitude growth rate predicted by the mFS model, respectively.

be expressed as

$$\dot{a}^+_{2,ls} = \dot{a}^-_{2,fs} + \Delta\dot{a}_{wni}, \tag{3.9}$$

where

$$\Delta\dot{a}_{wni} = ka^-_{2,fs}\left[\frac{1-A_2}{2}\left(1+\frac{v_2^{rw}+\Delta u_1}{v_2^{is}-\Delta u_1}\right)(u_2-\Delta u_1-\Delta u_2) + \Delta u_2\frac{1+A_2}{2}\left(1-\frac{v_2^{ts}-\Delta u_1}{v_2^{is}-\Delta u_1}\right)\right] \tag{3.10}$$

represents $\Delta\dot{a}$ predicted by the WNi model; $\dot{a}^-_{2,fs}$ and $a^-_{2,fs}$ correspond to $\dot{a}^-_2$ and the pre-reshock amplitude (a^-_2) predicted by the FS model, respectively; v_2^{rw} and u_2 denote the velocities of RW_2 and the fluid behind IS_2, respectively; A_2 represents the post-reshock Atwood number.

Values of $\dot{a}^+_2$ extracted from experiments ($\dot{a}^+_{2,e}$) and predicted by the LS model are presented in table 3. It can be observed that the LS model reasonably forecasts $\dot{a}^+_{2,e}$ for cases 0.36-553, 0.36-1043 and 0.67-235, whereas it performs poorly in predicting $\dot{a}^+_{2,e}$ for cases 0.67-566, 0.83-202 and 0.83-529. The failure of the LS model for case 0.67-566 should be attributed to the fact that ka^-_2 no longer satisfies the small-amplitude criterion, which is a fundamental assumption for the validity of the WNi model. Extensive research (Rikanati *et al.* 2003; Dimonte & Ramaprabhu 2010; Probyn *et al.* 2021; Wang *et al.* 2023*a*,*b*) has demonstrated that the high initial amplitude leads to the practical linear amplitude growth rate being lower than the predictions from models deduced based on the small-amplitude assumption – a phenomenon generally referred to as the high-amplitude effect. Several reduction factors have been proposed to describe this effect (Rikanati *et al.* 2003; Dimonte & Ramaprabhu 2010; Probyn *et al.* 2021; Wang *et al.* 2023*b*). Among them, the one proposed by Dimonte & Ramaprabhu (2010) (R_{dr}) has been demonstrated to effectively describe the high-amplitude effect on the evolution of a once-shocked heavy–light interface (Wang *et al.* 2023*a*). In contrast, for case 0.83-202, where ka^-_2 still satisfies the small-amplitude criterion, the failure of the LS model should be attributed to the fact that the FS model loses accuracy under high $|A_1|$ conditions, as demonstrated in § 3.2. For case 0.83-529, the failure of the LS model results from the combined influence of the high-amplitude effect and the limitation of the FS model.

https://doi.org/10.1017/jfm.2025.10828 Published online by Cambridge University Press

Here, we propose a modified model (mLS model) to predict $\dot{a}_2^+$ by combining the linear superposition principle, WNi model, mFS model and R_{dr}, expressed as

$$\dot{a}_{2,mls}^+ = \dot{a}_{2,mfs}^- + \Delta\dot{a}_{wni} \times R_{dr} = \dot{a}_{2,mfs}^- + \frac{\Delta\dot{a}_{wni}}{1 + \left(|ka_{2,mfs}^-|/3\right)^{4/3}}, \tag{3.11}$$

where

$$\Delta\dot{a}_{wni} = ka_{2,mfs}^- \left[\frac{1 - A_2}{2} \left(1 + \frac{v_2^{rw} + \Delta u_1}{v_2^{is} - \Delta u_1} \right) (u_2 - \Delta u_1 - \Delta u_2) + \Delta u_2 \frac{1 + A_2}{2} \left(1 - \frac{v_2^{ts} - \Delta u_1}{v_2^{is} - \Delta u_1} \right) \right], \tag{3.12}$$

and $\dot{a}_{2,mfs}^-$ and $a_{2,mfs}^-$ correspond to $\dot{a}_2^-$ and a_2^- predicted by the mFS model, respectively. As presented in table 3, the mLS model is capable of accurately predicting the linear amplitude evolution of a twice-shocked heavy–light interface under diverse A_1 and Δt conditions.

3.3.2. *Complete amplitude evolution*

Understanding the post-reshock linear amplitude evolution is essential. However, achieving a full-process prediction of the twice-shocked interface evolution remains a more desirable objective. Existing models, including the Mik-L, Cha-L, LS and mLS models, are limited to predicting only $\dot{a}_2^+$, without capturing the full temporal evolution. We therefore aim to develop a theoretical model that accurately describes the complete post-reshock evolution. Analogous to the development of a once-shocked interface, the evolution of a twice-shocked interface can be broadly divided into the shock-compression stage, start-up stage, linear stage, weakly nonlinear stage, strongly nonlinear stage and turbulent mixing stage. In this study, we focus exclusively on the evolution preceding the strongly nonlinear stage. The time-varying amplitude growth rate and amplitude of the twice-shocked interface are represented by $\dot{a}_2(t)$ and $a_2(t)$, respectively. The details of the model construction are provided below.

Shock-compression stage: The velocity of IS_2 relative to the once-shocked interface is typically much greater than $\dot{a}_2^-$. Consequently, as IS_2 propagates across the interface, the interface can be approximated as moving with velocity Δu_1 without undergoing any self-evolution. Accordingly, the duration of the shock-compression stage $(t_3 - \Delta t)$ and $a_2(t)$ in this stage can also be predicted using the R model:

$$t_3 - \Delta t = 2a_{2,mfs}^- / \left(v_2^{is} - \Delta u_1\right), \tag{3.13}$$

$$a_2(t) = a_{2,mfs}^- - \Delta u_2 \left(t - \Delta t\right)/2. \tag{3.14}$$

Start-up stage: The twice-shocked interface enters the start-up evolution stage ($t_3 < t < t_4$) once IS_2 has completely traversed the interface. Following the idea of linear superposition, the start-up evolution of the twice-shocked interface is considered as a process wherein $\dot{a}_2(t)$ varies from $\dot{a}_2^-$ to $\dot{a}_2^+$ under the drive of pressure perturbations introduced by the perturbed TS_2 and RW_2. Accordingly, the duration of the start-up process of the twice-shocked interface $(t_4 - t_3)$ and $\dot{a}_2(t)$ in this stage can be described

https://doi.org/10.1017/jfm.2025.10828 Published online by Cambridge University Press

by the reformulated Li model:

$$t_4 - t_3 = \frac{1}{k}\left(\frac{1 - A_2}{v_2^{rw} + \Delta u_1 + \Delta u_2} + \frac{1 + A_2}{v_2^{ts} - \Delta u_1 - \Delta u_2}\right), \tag{3.15}$$

$$\dot{a}_2(t) = \dot{a}_2^- + \frac{2\,\Delta\dot{a}}{(1 + A_2)\coth\left(kL_2^{ts}\right) + (1 - A_2)\coth\left(kL_2^{rw}\right)}, \tag{3.16}$$

where L_2^{ts} and L_2^{rw} denote the displacements of TS_2 and RW_2, respectively, which can be expressed as

$$\begin{cases} L_2^{ts} = \left(v_2^{ts} - \Delta u_1 - \Delta u_2\right)(t - t_3), \\ L_2^{rw} = \left(v_2^{rw} + \Delta u_1 + \Delta u_2\right)(t - t_3). \end{cases} \tag{3.17}$$

Linear stage: Similarly, the linear evolution stage of the twice-shocked interface is considered to have a negligible duration, during which $\dot{a}_2$ remains constant at $\dot{a}_2^+$. The mLS model, which has been validated earlier, is employed to predict $\dot{a}_2^+$. Specifically, $\dot{a}_2^-$ and $\Delta\dot{a}$ in (3.16) are given by $\dot{a}_{2,mfs}^-$ and $\Delta\dot{a}_{wni} \times R_{dr}$, respectively.

Weakly nonlinear stage: Currently, there is still a lack of nonlinear models specifically proposed for the twice-shocked interface. Our previous study (Wang *et al.* 2022) demonstrated that for a light–heavy interface configuration, the evolution of a twice-shocked interface can be reasonably predicted by models developed for once-shocked interfaces, provided that the reshock occurs prior to the strongly nonlinear stage. This suggests that it is potentially feasible to treat a twice-shocked heavy–light interface as a once-shocked one with equivalent post-shock amplitude and linear growth rate. Based on this idea, the weakly nonlinear evolution of twice-shocked heavy–light interfaces with varying A is also described using the mSEA model reformulated as

$$\begin{cases} \dot{a}_2(t) = \left[\dot{a}_2^b(t) + \dot{a}_2^s(t)\right]/2, \\ \dot{a}_2^{b/s}(t) = \dot{a}_{2,mls}^+ \dfrac{1 + k\dot{a}_{2,mls}^+(t - t_4)}{1 + (2 \mp |A_2|)(1.07 \pm |A_2|)k\dot{a}_{2,mls}^+(t - t_4) + \dfrac{1 \pm |A_2|}{1 + |A_2|}\dfrac{1}{2\pi C_2}k^2\dot{a}_{2,mls}^{+2}(t - t_4)^2}, \end{cases} \tag{3.18}$$

where C_2 is given by $1/3\pi$ for cases with $|A_2| \geqslant 0.5$, and $1/2\pi$ for cases with $|A_2| \to 0$. For clarity, the combination of (3.11)–(3.18) is hereafter referred to as the DS model. As illustrated in figure 8, the DS model offers accurate predictions for the amplitude evolution from the instant IS_2 hits the once-shocked interface to the weakly nonlinear evolution stage of the twice-shocked interface under diverse A and Δt conditions.

In conclusion, two models, namely the mFS and DS models, have been developed based on existing theoretical models and physically justified assumptions. Experimental validation confirms that, when combined, they can reliably predict the complete perturbation evolution of S-RMI across a wide range of A. In the following, we will employ these models to achieve the controllable suppression of RMI via a same-side reshock under low, moderate and high $|A|$ conditions.

4. Experimental realisation of instability suppression

Building upon the possibility analysis of Mikaelian (1985), Zhai *et al.* (2025) systematically discussed the possible amplitude evolution patterns. However, both

https://doi.org/10.1017/jfm.2025.10828 Published online by Cambridge University Press

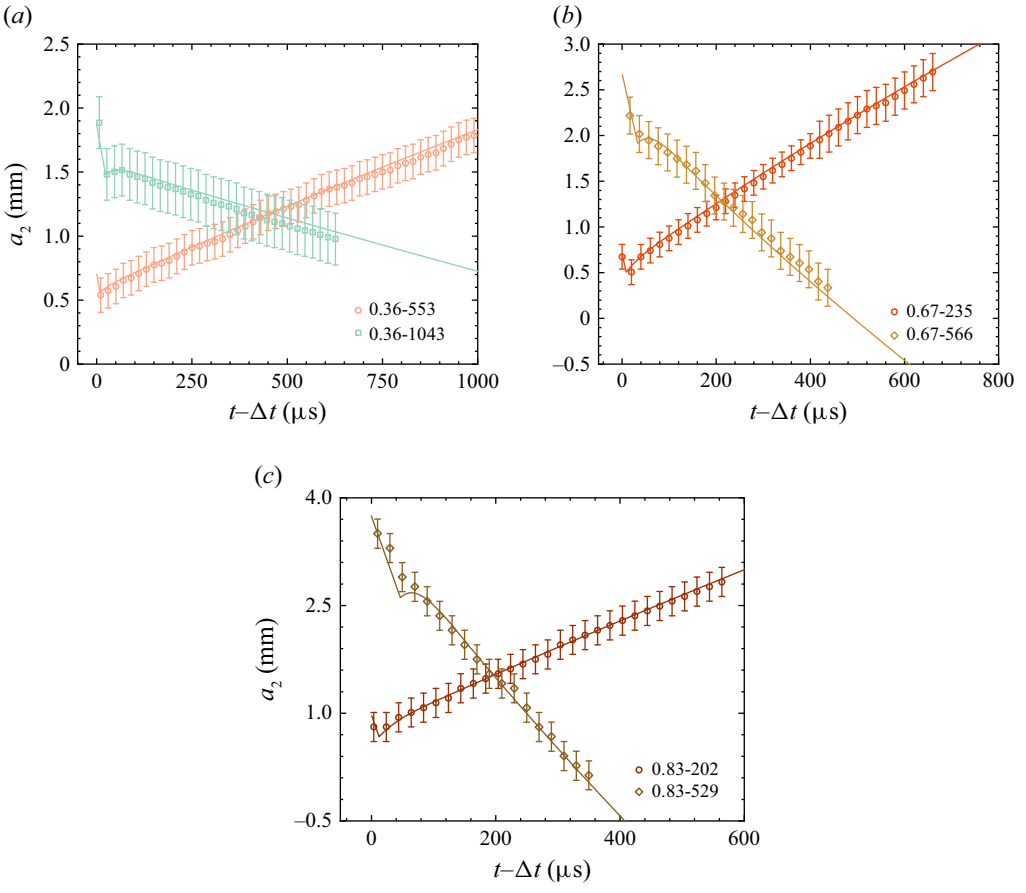


Figure 8. Amplitude evolution of twice-shocked interface under diverse A and Δt conditions. Symbols and solid lines denote experimental results and theoretical predictions by the DS model, respectively.

analyses are based on the assumption of incompressibility. In certain compressible scenarios, such as RMI at a light–heavy interface where the light gas exhibits strong compressibility, the heavy gas is weakly compressible, and the initial density contrast is moderate, an Atwood-number-reversal phenomenon (i.e. A_1 possesses an opposite sign to A_0) may occur (Mikaelian 1994). Under such compressible conditions, the previous incompressible analyses become less rigorous. A detailed discussion of the perturbation evolution possibilities in a compressible two-co-propagating-shock system is provided in Appendix B.

In the present experiments, since the heavy gas (SF_6) is characterised by a relatively high compressibility, and the light gas (Kr, air and He) by a relatively low compressibility, A_1 retains the same sign as A_0. In other words, the present experiments correspond to compressible S-RMI scenarios without Atwood-number reversal. According to Appendix B, the analyses by Mikaelian (1985) and Zhai *et al.* (2025) for incompressible S-RMI remain valid under the present experimental conditions: seven distinct evolution patterns arise, depending on the relative signs and magnitudes of $\dot{a}_2^-$ and $\dot{a}_2^+$, as depicted in figure 9. Among them, the suppression of RMI growth ($|\dot{a}_2^+| < \dot{a}_2^-$) occurs in possibilities III-HL, IV-HL and V-HL. In particular, in possibility IV-HL, where $\dot{a}_2^+ = 0$, the freeze-out phenomenon occurs.

https://doi.org/10.1017/jfm.2025.10828 Published online by Cambridge University Press

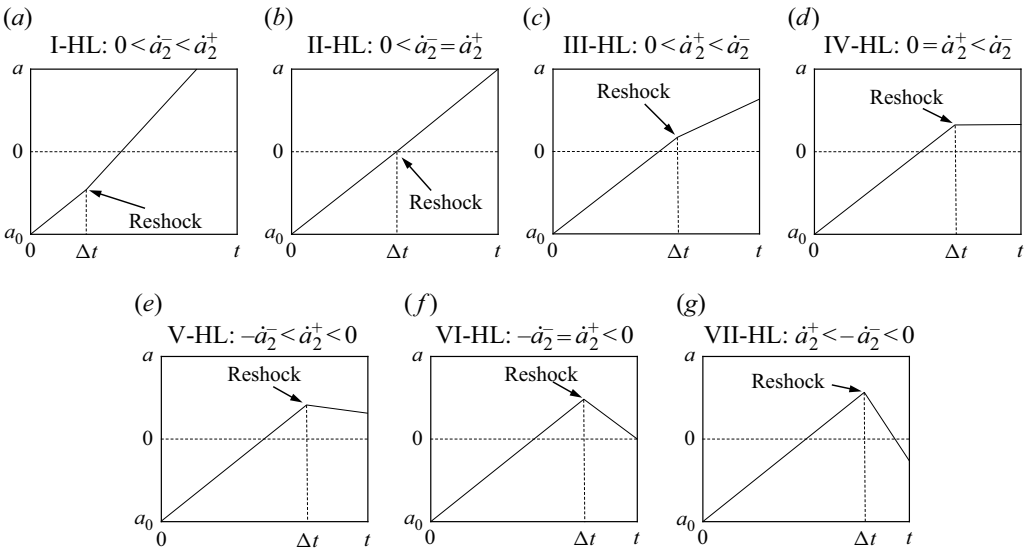


Figure 9. Schematics of seven possibilities for S-RMI at an initial heavy–light interface without Atwood-number reversal ($A_0 < 0$ and $A_1 < 0$).

Based on the mFS and DS models, and the general 1-D experimental parameters presented in table 1, theoretical lines corresponding to possibilities II-HL, IV-HL and VI-HL in the (λ, Δt) plane are calculated. The results for cases with A_1 values -0.36, -0.67 and -0.83 are depicted in figures 10(*a–c*), respectively. These lines, referred to as the acceleration line, freeze-out line and reversal line, respectively, partition the plane into four regions, corresponding to possibilities I-HL, III-HL, V-HL and VII-HL. Figure 10 indicates that by keeping the gas combination, initial perturbation and shock intensities constant, the twice-shocked interface evolution can be manipulated by varying Δt. The six experimental cases with different A and Δt, discussed in § 3, are plotted as open circles in figure 10. For the scenario with low $|A|$, cases 0.36-553 and 0.36-1043 correspond to possibilities III-HL and V-HL, respectively. For the scenario with moderate (high) $|A|$, case 0.67-235 (case 0.83-202) corresponds to possibility III-HL. To realise all three possibilities of instability suppression in each A scenario, five additional experimental runs corresponding to possibilities without existing experiments are conducted: IV-HL for the low $|A|$ scenario, and IV-HL and V-HL for moderate and high $|A|$ scenarios. These runs are represented by solid circles in figure 10.

Figure 11 presents the schlieren images for all nine experimental cases in which the amplitude growth is theoretically predicted to be suppressed by the same-side reshock. In all cases, the interface maintains a quasi-single-mode profile before reshock, indicating that the reshock occurs prior to the strongly nonlinear stage. The complete interface amplitude evolution for these nine cases throughout the effective experimental duration is presented in figure 12, along with the predictions from the mFS and DS models. It is evident that the post-reshock amplitude evolution rate is significantly lower than the pre-reshock one, and all theoretical predictions are in excellent agreement with the experimental results, indicating that all three possibilities for suppressing the RMI growth are achieved under low, moderate and high $|A|$ conditions. Overall, the suppression and freeze-out of the RMI growth via a same-side reshock are achievable and predictable under diverse A conditions.

https://doi.org/10.1017/jfm.2025.10828 Published online by Cambridge University Press

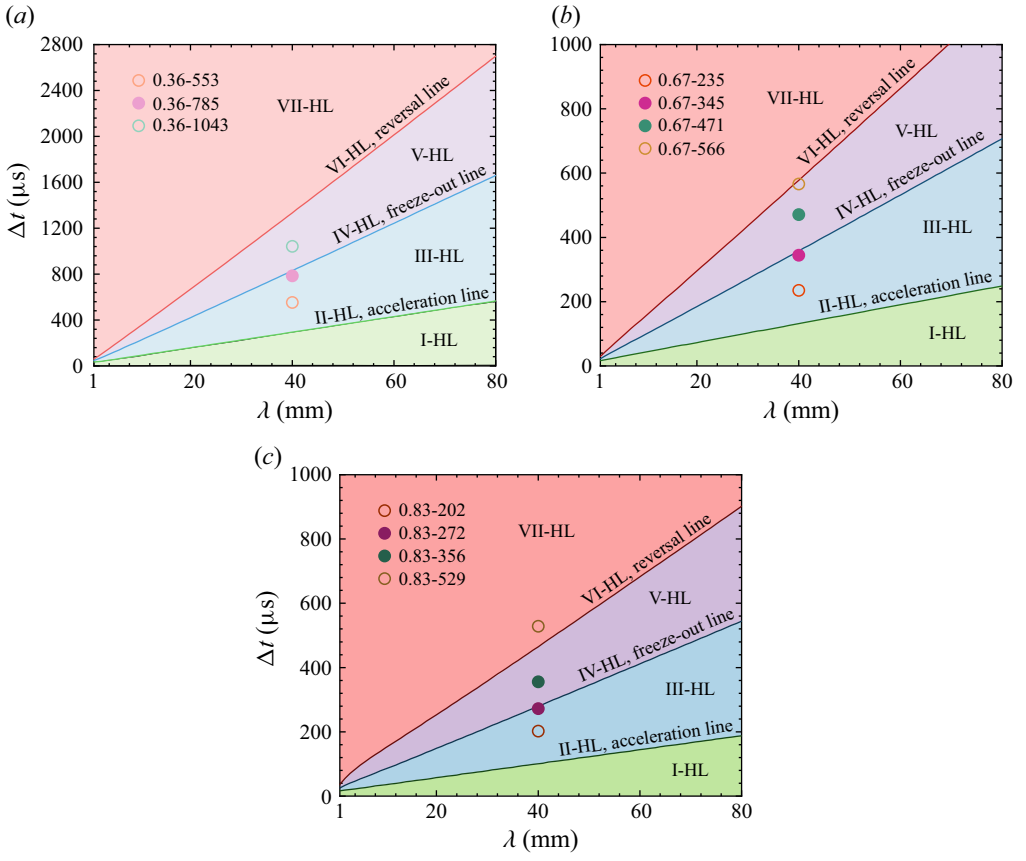


Figure 10. Parameter conditions corresponding to each perturbation evolution possibility for scenarios with various A. Open circles denote the experimental cases that have been discussed in § 3, whereas solid circles represent the supplementary experimental runs.

5. Conclusions and perspective

This study explores the evolution law and suppression strategy of the Richtmyer–Meshkov instability (RMI) induced by two co-propagating shock waves (S-RMI) across a broad range of Atwood numbers, integrating theoretical and experimental approaches. Experimentally, two co-propagating shocks with controllable time intervals (Δt) and intensities are generated using a dedicated shock-tube facility (Wang *et al.* 2022), while well-defined initial interfaces with varying Atwood numbers are produced via an improved soap-film technique. Previously developed models (Zhai *et al.* 2025) describing the complete evolution of a once-shocked interface and the linear growth of a twice-shocked interface are evaluated under diverse post-first-shock Atwood numbers (-0.36, -0.68 and -0.83), and further refined based on detailed analyses of their limitations. Furthermore, an analytical model for describing the complete evolution of a twice-shocked interface (DS model) is developed by comprehensively considering the shock-compression, start-up, linear and weakly nonlinear evolution processes. Shock-tube experiments with various Atwood numbers and Δt values demonstrate that the combination of the refined models and DS model enables, for the first time, an accurate prediction of the complete evolution of S-RMI. Based on these models and the general one-dimensional flow information,

https://doi.org/10.1017/jfm.2025.10828 Published online by Cambridge University Press

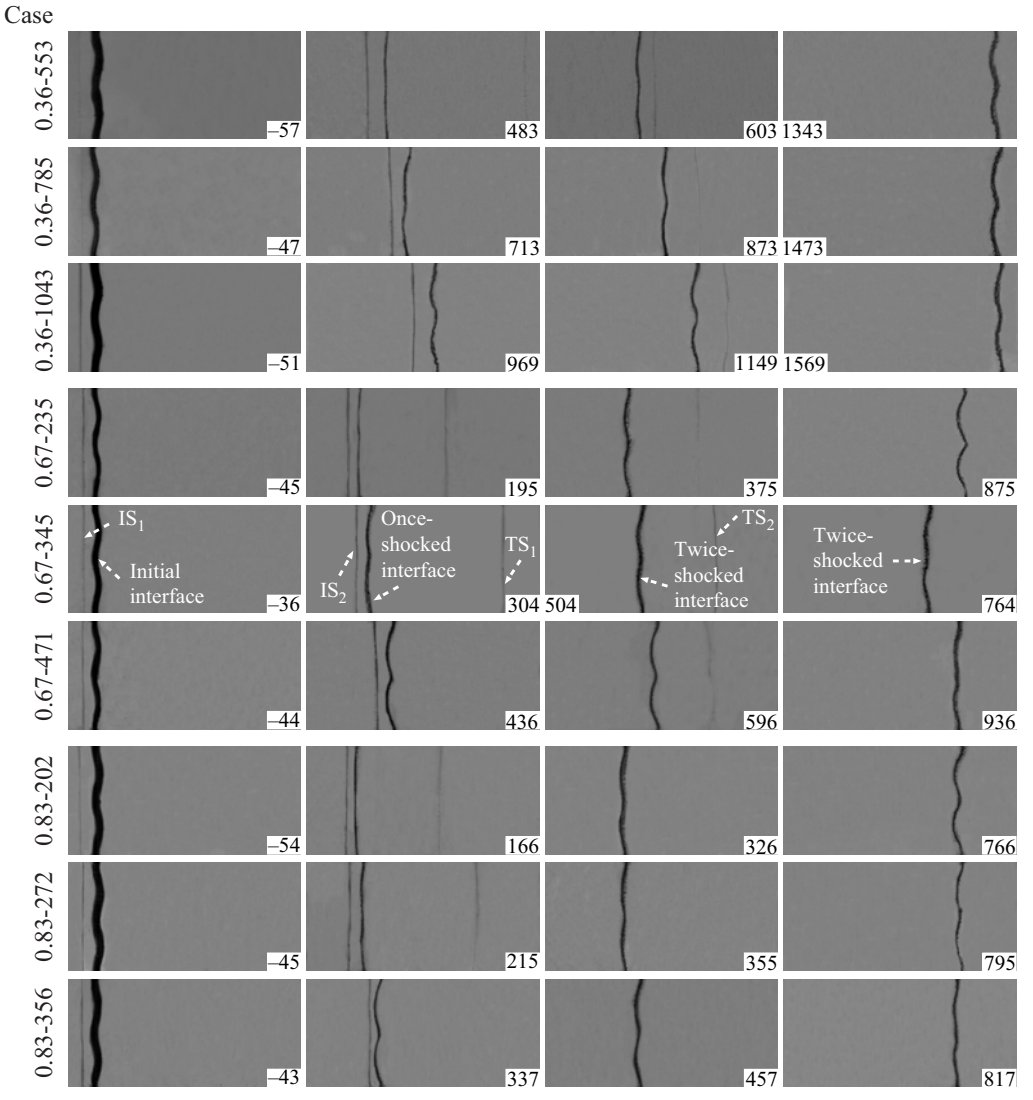


Figure 11. Schlieren photographs of experimental cases in which the amplitude growth is theoretically predicted to be suppressed by the same-side reshock.

parameter conditions for manipulating the RMI growth are identified. Nine validation experiments with diverse combinations of Atwood numbers and Δt confirm that the suppression and freeze-out of the RMI growth via a same-side second impact are feasible and predictable across a wide range of Atwood numbers.

This study may offer some insights into the suppression of hydrodynamic instabilities in inertial confinement fusion (ICF) through a same-side reshock. Specifically, by optimising material densities and shock timings within the framework of global implosion dynamics, the early-time perturbation growth induced by RMI could potentially be suppressed through reshock, thereby mitigating the development of the Rayleigh–Taylor (RT) instability (Rayleigh 1883; Taylor 1950) in the subsequent deceleration phase.

https://doi.org/10.1017/jfm.2025.10828 Published online by Cambridge University Press

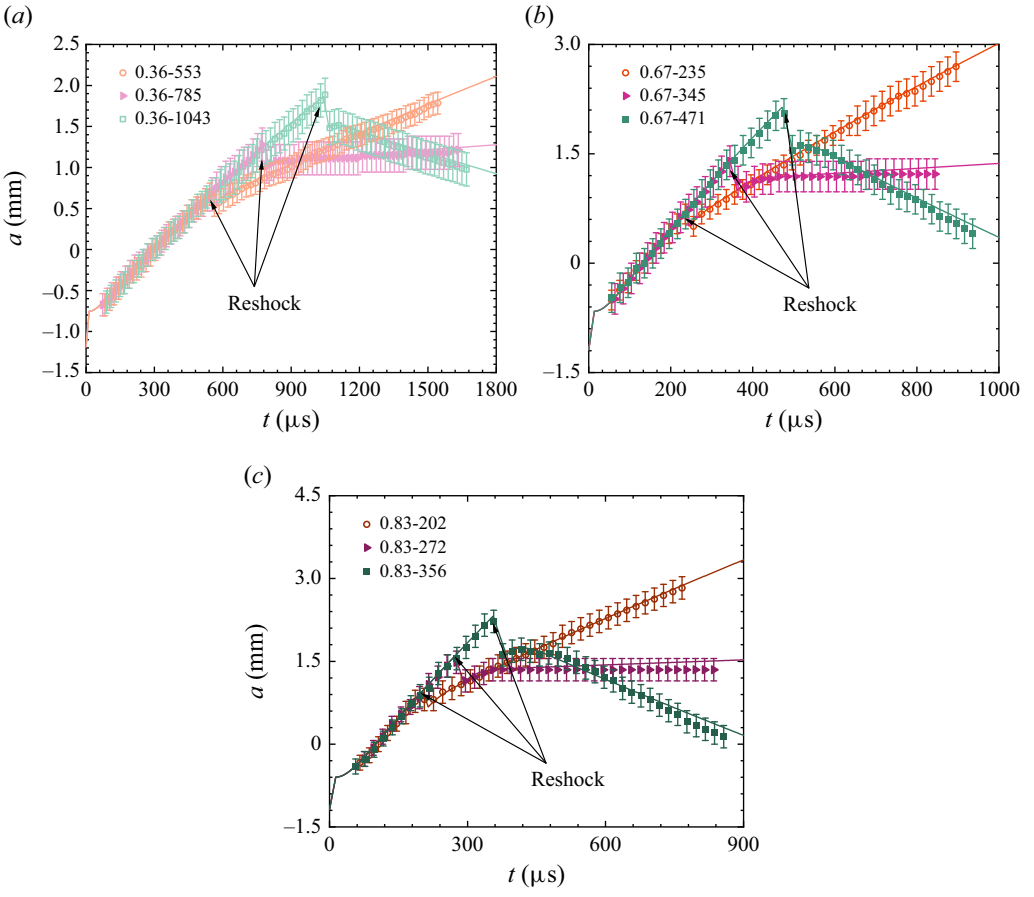


Figure 12. Complete interface amplitude evolution for nine experimental cases in which the amplitude growth is theoretically predicted to be suppressed by the same-side reshock. Solid lines represent the theoretical predictions from the mFS and DS models.

However, we acknowledge that our consideration of a single-mode gaseous interface in planar geometry represents a considerable simplification of the actual ICF scenario. In ICF, the hydrodynamic instabilities arise at multi-material interfaces exhibiting multi-mode perturbations and are driven by co-propagating convergent shock waves. Although the present models have been validated by 11 experiments spanning a range of Atwood numbers and Δt values, they are not expected to accurately describe more complex flows owing to the presence of additional physical mechanisms. To explore the instability suppression strategies under conditions that more closely resemble those in actual ICF scenarios, we propose the following three future research directions, within which the current models will be further evaluated and refined to address increased physical complexity.

First, consider S-RMI in convergent geometry. In ICF, a convergent geometry implosion scheme is adopted to achieve maximum energy density for a given driver energy. Compared with RMI in planar geometry, RMI in convergent geometry involves additional physical mechanisms. Bell (1951) and Plesset (1954) analysed the early-time interface instability in convergent geometry, and demonstrated that the radial movement of the interface affects perturbation growth, a phenomenon now referred to as the Bell–Plesset

https://doi.org/10.1017/jfm.2025.10828 Published online by Cambridge University Press

(BP) effect. Additionally, unlike in planar geometry where the interface typically maintains a constant velocity, the interface in convergent geometry generally experiences acceleration or deceleration, thereby giving rise to the RT effect (Lombardini, Pullin & Meiron 2014; Ding *et al.* 2017*b*; Samulski *et al.* 2022). In S-RMI within a convergent geometry, the BP effect, RT effect and same-side reshock are intrinsically coupled, thereby significantly increasing the physical complexity. A novel facility capable of generating two co-propagating convergent shock waves is currently under development. This platform will enable detailed investigations into the evolution mechanisms and potential manipulation strategies for S-RMI in convergent geometry.

Second, consider S-RMI at multi-mode interfaces. In ICF, multi-mode perturbations inevitably arise at the interfaces separating different layers due to the manufacturing defects and material inhomogeneities. Furthermore, critical engineering features, such as the fill tube and the supporting membrane, serve as additional sources of the multi-mode perturbations at the target interfaces (Zhou *et al.* 2025). Therefore, understanding and further suppressing the instability on multi-mode interfaces are necessary and of significant scientific importance. In future work, we will explore the evolution mechanisms and manipulation strategies of S-RMI at multi-mode interfaces, with detailed consideration of the modal coupling and competition.

Third, consider S-RMI at multi-material interfaces. The present study focuses solely on the evolution of S-RMI at gas–gas interfaces. However, ICF targets generally involve multi-material interfaces, such as gas–solid and solid–solid ones. The presence of non-gaseous materials introduces additional physical mechanisms affecting RMI evolution. For example, at gas–hydrogel interfaces, the viscosity and elasticity of the hydrogel can influence RMI evolution, which manifest through viscous dissipation and elastic energy storage, respectively. Future work will investigate the mechanisms and manipulation of S-RMI when non-gaseous materials are present on one or both sides of the interface.

Acknowledgements. The authors sincerely appreciate the reviewers for their valuable suggestions.

Funding. This work was supported by the National Natural Science Foundation of China (nos 12388101, 12472228, 12372281 and 12027801), the Young Elite Scientists Sponsorship Programme by CAST (no. 2023QNRC001), and the Strategic Priority Research Programme of the Chinese Academy of Science (XDB1100120).

Declaration of interests. The authors report no conflict of interest.

Appendix A. Comparison between validation experiments

To evaluate the reliability and repeatability of the experiments, three experimental runs are conducted for each gas combination, following identical procedures. Notably, among three runs with the same gas combination, the first two have similar Δt, while the third has a relatively longer Δt, to verify whether the variation in Δt would affect the general 1-D flow parameters.

The trajectories and velocities of shock waves and interface, extracted from different experimental runs, are presented in figure 13 and table 4, respectively. These results demonstrate that the 1-D flow parameters are highly consistent across different runs with the same gas combination, confirming the reliability of the experimental approach.

Appendix B. Possible evolution patterns in a compressible two-co-propagating-shock system

In the pioneering work by Mikaelian (1994) on the influence of compressibility on RMI, it was proposed that under certain conditions, such as when the shock intensity is high and

https://doi.org/10.1017/jfm.2025.10828 Published online by Cambridge University Press

Gas combination	Serial number	v_1^{is}	v_1^{ts}	Δu_1	v_2^{is}	v_2^{ts}	Δu_2
SF_6–Kr	1	175.15	277.32	64.34	223.73	335.89	34.01
	2	174.87	273.07	64.75	225.32	334.27	34.79
	3	175.69	274.31	64.44	225.69	333.33	33.65
SF_6–air	1	175.08	395.96	77.54	239.73	469.56	47.04
	2	174.12	394.76	77.81	239.15	470.21	46.51
	3	174.66	395.82	78.08	239.53	469.18	46.09
SF_6–He	1	175.15	592.81	86.96	247.57	—	49.85
	2	176.13	592.83	86.19	248.74	—	50.50
	3	175.33	592.95	85.93	248.19	—	50.74

Table 4. Key parameters of nine validation experiments for evaluating the reliability of the experimental methods: v_1^{is} and v_1^{ts} (v_2^{is} and v_2^{ts}) are velocities of IS_1 and TS_1 (IS_2 and TS_2), respectively; Δu_1 and Δu_2 are jump velocities of the interface induced by IS_1 and IS_2, respectively. Unit of all parameters representing velocity is m s^{-1}.

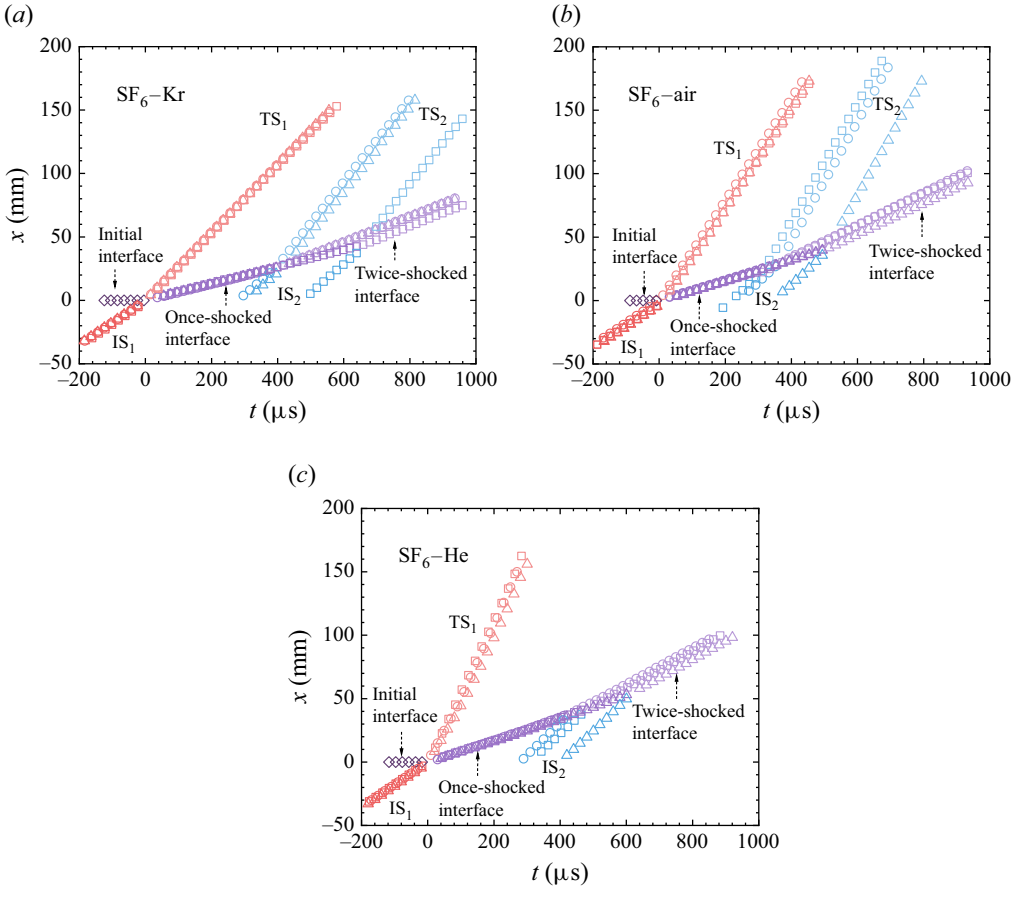


Figure 13. Trajectories of shocks and interface extracted from nine validation experiments. Diverse symbols (circle, square and triangle) represent different experimental runs with the same gas combination: (*a*) SF_6–Kr, (*b*) SF_6–air, (*c*) SF_6–He.

https://doi.org/10.1017/jfm.2025.10828 Published online by Cambridge University Press

the light (heavy) fluid is strongly (weakly) compressible, the Atwood-number reversal, a phenomenon that A_0 and A_1 have opposite signs (i.e. $A_0 > 0$ but $A_1 < 0$, or $A_0 < 0$ but $A_1 > 0$), may occur. Although this phenomenon is challenging to realise experimentally due to the physical constraints of available gases, it nonetheless provides additional possibilities for manipulating RMI via a same-side reshock. In the following, analysis is performed to clarify the possible amplitude evolution patterns in a compressible two-co-propagating-shock system, considering scenarios with and without Atwood-number reversal, as well as special cases with $A_0 \neq 0$ but $A_1 = 0$. To facilitate analysis, following the conventions of previous studies (Mikaelian 1985; Zhai *et al.* 2025), we assume that a_0 is positive for an initial light–heavy interface, and negative for an initial heavy–light one.

B.1 *Initial light–heavy interface* ($A_0 > 0$)

An initial light–heavy interface subjected to a shock wave would continue to evolve in the same phase, i.e. no phase inversion would occur. Based on the A_1 value, there are three distinct scenarios: $A_1 > 0$, $A_1 = 0$ and $A_1 < 0$, which are analysed separately below.

B.1.1 *Case* $A_0 > 0$ *and* $A_1 > 0$

For this scenario, the relative orientations of the shock-induced pressure gradient and the interfacial density gradient in the first impact and reshock are identical, such that the vorticity generated by the reshock possesses the same sign as that produced by the first shock. Therefore, for an initial light–heavy interface without Atwood-number reversal, a same-side reshock can only promote the instability (possibility I-LH), consistent with the analysis by Mikaelian (1985) and Zhai *et al.* (2025) for incompressible S-RMI.

B.1.2 *Case* $A_0 > 0$ *and* $A_1 = 0$

If the light and heavy gases are highly and weakly compressible, respectively, and the initial density contrast is moderate, then A_1 can approach zero or even become negative, as proposed by Mikaelian (1994). For the scenario with $A_1 = 0$, since there is no density gradient on the once-shocked interface, the reshock cannot deposit additional vorticity and is therefore expected to exert no influence on the instability (possibility II-LH).

B.1.3 *Case* $A_0 > 0$ *and* $A_1 < 0$

In this case, due to the differing relative orientations of the pressure and density gradients in the first impact and reshock, the vorticity deposited by reshock carries an opposite sign to that induced by the first shock. In other words, $\Delta\dot{a}$ is of opposite sign to $\dot{a}_2^-$. Depending on the relative signs and magnitudes of $\dot{a}_2^-$ and $\dot{a}_2^+$ ($= \dot{a}_2^- + \Delta\dot{a}$), five distinct evolution scenarios arise, as illustrated in figure 14 and described sequentially below.

Possibility III-LH: $|\Delta\dot{a}| < \dot{a}_2^-$ and $0 < \dot{a}_2^+ < \dot{a}_2^-$, i.e. the reshock weakens the instability triggered by the first shock while preserving the original growth trend.

Possibility IV-LH: $|\Delta\dot{a}| = \dot{a}_2^-$ and $\dot{a}_2^+ = 0$, i.e. the reshock eliminates the instability at the once-shocked interface, resulting in a freeze-out phenomenon.

Possibility V-LH: $\dot{a}_2^- < |\Delta\dot{a}| < 2\dot{a}_2^-$ and $-\dot{a}_2^- < \dot{a}_2^+ < 0$, i.e. the reshock not only attenuates the instability but also reverses the trend of perturbation growth.

Possibility VI-LH: $|\Delta\dot{a}| = 2\dot{a}_2^-$ and $\dot{a}_2^+ = -\dot{a}_2^-$, i.e. the reshock reverses the evolution trend of RMI growth without changing its rate.

Possibility VII-LH: $|\Delta\dot{a}| > 2\dot{a}_2^-$ and $\dot{a}_2^+ < -\dot{a}_2^-$, i.e. the reshock both reverses the perturbation growth trend and enhances the instability.

https://doi.org/10.1017/jfm.2025.10828 Published online by Cambridge University Press

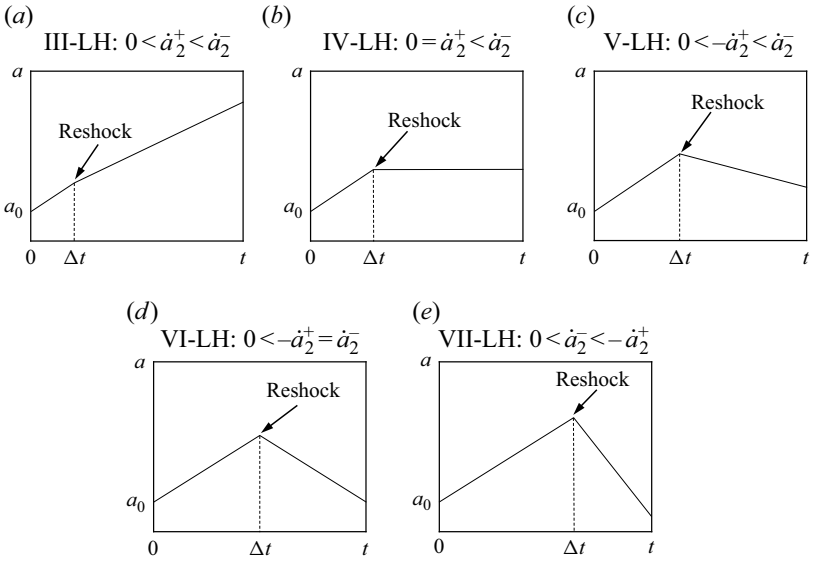


Figure 14. Schematics of five possibilities for S-RMI at an initial light–heavy interface with Atwood-number reversal ($A_0 > 0$ and $A_1 < 0$).

B.2 *Initial heavy–light interface* ($A_0 < 0$)

For an initial heavy–light interface subjected to a shock wave, it would undergo a phase-inversion process, i.e. the amplitude first decreases over time, becoming zero, then grows in the opposite phase. Similarly, in terms of A_1, there are three distinct scenarios: $A_1 < 0$, $A_1 = 0$ and $A_1 > 0$, each of which is analysed separately below.

B.2.1 *Case* $A_0 < 0$ *and* $A_1 < 0$

Since A_0 and A_1 share the same sign, if reshock occurs during the phase-inversion process, then the relative orientations of the pressure and density gradients in the first impact and reshock are identical. As a result, the reshock would enhance the instability (possibility I-HL), as illustrated in figure 9(*a*). In contrast, if the reshock occurs exactly at the moment the phase inversion is completed, then the interface is planar, leading to collinearity between the pressure and density gradients. In this case, the reshock would not affect the instability (possibility II-HL), as illustrated in figure 9(*b*). If the reshock occurs after phase inversion, then the relative orientations of the pressure and density gradients in the first impact and reshock are opposite. For this scenario, there are five distinct possibilities (possibilities III-HL to VII-HL), depending on the relative signs and magnitudes of $\dot{a}_2^-$ and $\dot{a}_2^+$, as illustrated in figures 9(*c–g*). Details on these possibilities can be found in a previous work (Zhai *et al.* 2025) and thus are not repeated here.

B.2.2 *Case* $A_0 < 0$ *and* $A_1 = 0$

For an initial heavy–light interface, if the heavy and light gases are weakly and strongly compressible, respectively, and the density contrast is moderate, then the first impact may yield either $A_1 = 0$ or $A_1 > 0$. For the scenario with $A_1 = 0$, since the density gradient across the once-shocked interface vanishes, the reshock would not deposit additional vorticity regardless of its timing. Accordingly, the reshock is expected to have no influence on the instability (possibility VIII-HL).

https://doi.org/10.1017/jfm.2025.10828 Published online by Cambridge University Press

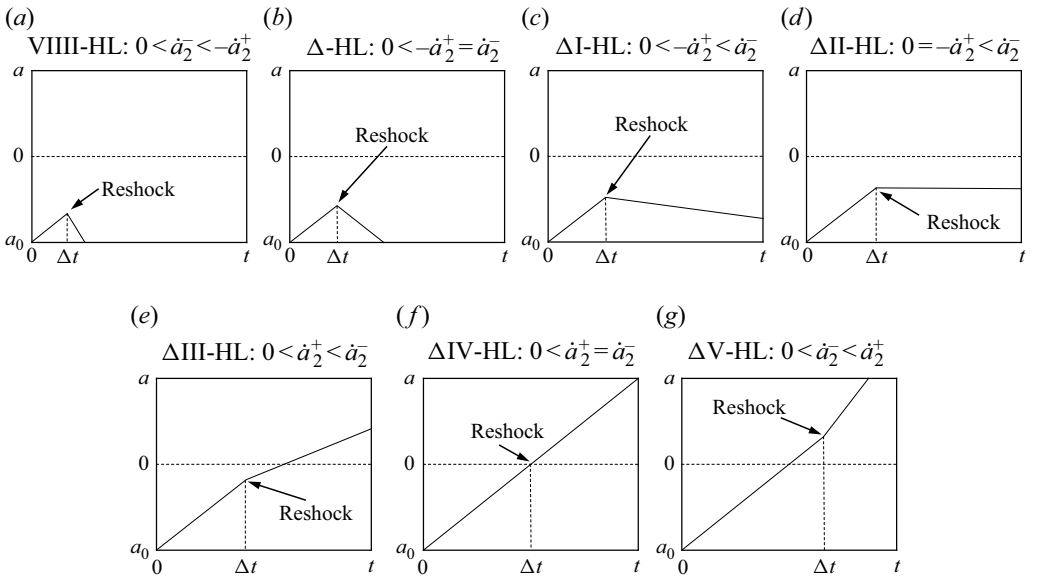


Figure 15. Schematics of seven possibilities for S-RMI at an initial heavy–light interface with Atwood-number reversal ($A_0 < 0$ and $A_1 > 0$).

B.2.3 *Case* $A_0 < 0$ *and* $A_1 > 0$

Since A_0 and A_1 have opposite signs, if reshock occurs during the phase-inversion process, then the relative orientations of the pressure and density gradients in the first impact and reshock are opposite. In other words, $\Delta\dot{a}$ has sign opposite to that of $\dot{a}_2^-$. Depending on the relative signs and magnitudes of $\dot{a}_2^-$ and $\dot{a}_2^+$, there are five possible evolution patterns, as illustrated in figures 15(*a–e*) and described sequentially below.

Possibility VIIII-HL: $|\Delta\dot{a}| > 2\dot{a}_2^-$ and $-\dot{a}_2^+ > \dot{a}_2^-$, i.e. the reshock promotes the instability induced by the first shock and simultaneously alters its evolution trend.

Possibility Δ-HL: $|\Delta\dot{a}| = 2\dot{a}_2^-$ and $-\dot{a}_2^+ = \dot{a}_2^-$, i.e. the reshock reverses the evolution trend of RMI growth without changing its rate.

Possibility ΔI-HL: $\dot{a}_2^- < |\Delta\dot{a}| < 2\dot{a}_2^-$ and $0 < -\dot{a}_2^+ < \dot{a}_2^-$, i.e. the reshock weakens the instability and concurrently alters the evolution trend.

Possibility ΔII-HL: $|\Delta\dot{a}| = \dot{a}_2^-$ and $\dot{a}_2^+ = 0$, i.e. the reshock eliminates the instability at the once-shocked interface, giving rise to a freeze-out phenomenon.

Possibility ΔIII-HL: $|\Delta\dot{a}| < \dot{a}_2^-$ and $\dot{a}_2^- > \dot{a}_2^+ > 0$, i.e. the reshock attenuates the instability without altering the evolution trend.

If reshock occurs precisely at the moment the phase inversion is completed, since the interface is planar, the pressure and density gradients are collinear. Consequently, the reshock would not deposit vorticity on the interface, thus does not contribute to the instability: possibility ΔIV-HL ($\Delta\dot{a} = 0$ and $\dot{a}_2^+ = \dot{a}_2^-$), illustrated in figure 15(*f*). In contrast, if reshock occurs after phase inversion, then the relative orientations of the pressure and density gradients in the first impact and reshock are identical. As a result, the reshock deposits vorticity of the same sign as that deposited by the first shock, and thus would promote the instability: possibility ΔV-HL ($\Delta\dot{a} > 0$ and $\dot{a}_2^+ > \dot{a}_2^-$), illustrated in figure 15(*g*).

Overall, for an initial light–heavy interface, there are seven possibilities: one without Atwood-number reversal, one with $A_1 = 0$, and five with Atwood-number reversal, depending on the relative signs and magnitudes of $\dot{a}_2^-$ and $\dot{a}_2^+$. In contrast, for an initial

https://doi.org/10.1017/jfm.2025.10828 Published online by Cambridge University Press

heavy–light interface, fifteen possibilities arise: seven without Atwood-number reversal, one with $A_1 = 0$, and seven with Atwood-number reversal, all categorised based on the relative signs and magnitudes of $\dot{a}_2^-$ and $\dot{a}_2^+$.

Appendix C. Evaluation on assumptions for model construction

During the interaction between IS_1 and the initial interface, rippled TS_1 and RW_1 are generated. Subsequently, RW_1 interacts with IS_2 and causes it to become perturbed, thereby further influencing the post-reshock evolution of the interface. In addition, the pressure, density and velocity fields behind the rippled TS_1 are non-uniform. The interaction of TS_2 with this non-uniform flow is expected to affect the RMI growth triggered on the twice-shocked interface. Given the complexity of the propagation and interaction of unsteady perturbed waves, it is highly challenging to provide a theoretical description of the influence of rippled IS_2 and non-uniform flow behind TS_1 on the interface evolution. Fortunately, the initial interface perturbation considered in this study satisfies the small-amplitude criterion. Accordingly, two simplifying assumptions are made in developing the model for the twice-shocked interface evolution. First, the influence of the rippled RW_1 on IS_2 is negligible, i.e. IS_2 can be treated as a planar shock. Second, the non-uniformities in the flow field behind TS_1 have a negligible influence on TS_2, i.e. the flow field ahead of TS_2 can be approximated as uniform. To evaluate these two assumptions, numerical simulations are conducted.

The numerical solver HOWD (Ding *et al.* 2017*a*) is employed to simulate the interaction between two co-propagating shock waves and a single-mode heavy–light interface. Its accuracy and reliability in capturing the RMI have been validated through various experiments (Ding *et al.* 2018; Feng *et al.* 2021; Wang *et al.* 2023*b*). The computational domain is a rectangle measuring 400 mm in length and 40 mm in height. The upper and lower boundaries are modelled as solid walls, whereas the others are treated as open. The grid resolution is guided by grid convergence studies conducted in previous works (Ding *et al.* 2018; Feng *et al.* 2021; Wang *et al.* 2023*b*). To ensure numerical accuracy while minimising computational cost, an initial mesh size of 0.1 mm is adopted. Six simulations, corresponding to the experimental cases discussed in § 3, have been performed. All initial conditions are kept consistent with those in the experiments. Notably, to highlight the perturbation of IS_2 caused by rippled RW_1 and the non-uniformities of the flow behind TS_1, a counterpart simulation assuming a flat initial interface is conducted for each case to serve as a reference.

C.1 *Perturbation of IS_2 induced by RW_1*

Using simulations with a flat initial interface as references, we introduce three parameters to quantify the perturbation of IS_2 induced by RW_1: pressure deviation $E_p = (p - p_0)/p_0$, density deviation $E_\rho = (\rho - \rho_0)/\rho_0$, and velocity deviation $E_u = (u - u_0)/u_0$. Here, p, ρ and u represent the pressure, density and velocity in simulations with a perturbed initial interface, respectively, while p_0, ρ_0 and u_0 denote the counterparts in the region between IS_2 and RW_1 in simulations with a flat initial interface, respectively.

The distributions of E_p, E_ρ and E_u shortly before reshock are presented in figure 16. It is observed that the flow features are highly related to Δt, as it influences the time intervals between the IS_2–RW_1 interaction and the reshock. In simulations with a relatively long Δt (cases 0.36-553, 0.36-1043, 0.67-566 and 0.83-529), the absolute values of E_p and E_ρ do not exceed 1 %, and those of E_u are below 2 % in the vicinity of IS_2. For simulations with relatively short Δt (cases 0.67-235 and 0.83-202), although the perturbations in the

https://doi.org/10.1017/jfm.2025.10828 Published online by Cambridge University Press

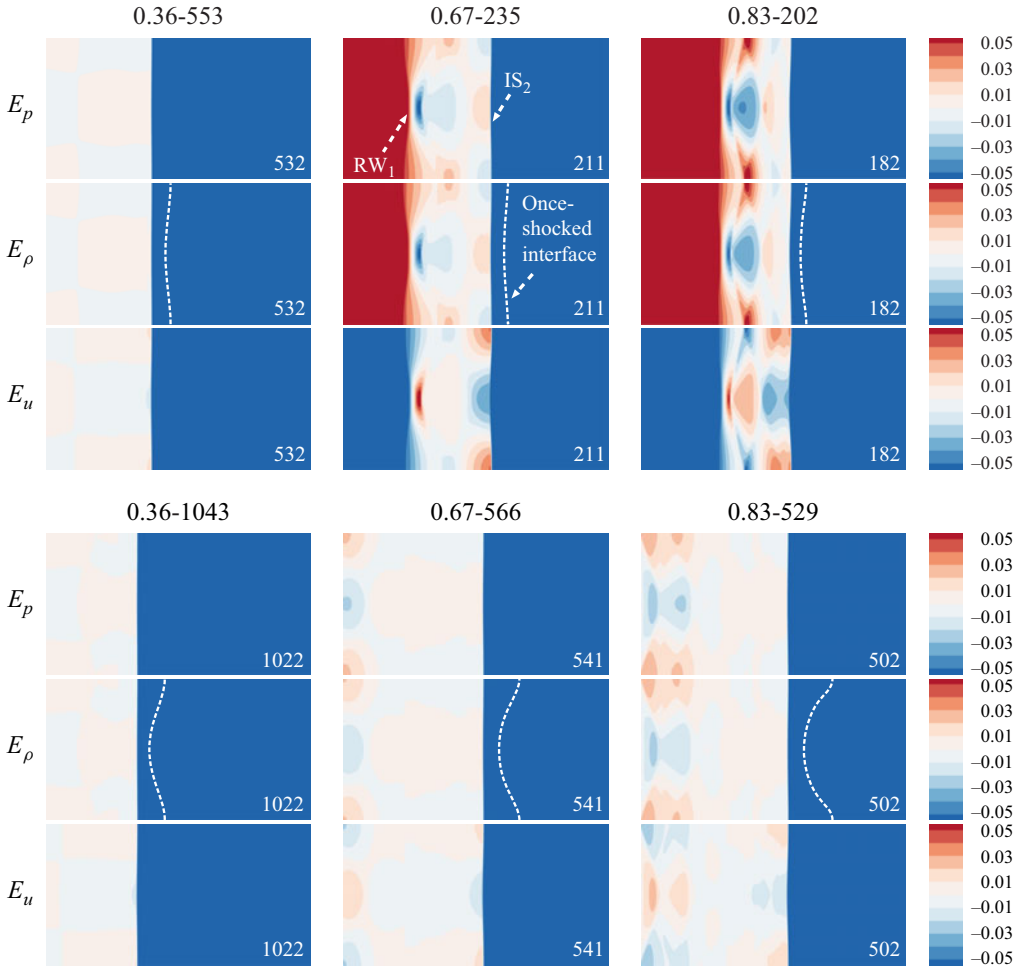


Figure 16. Distributions of E_p, E_ρ and E_u shortly before reshock in simulations labelled by the combination of $|A_1|$ and Δt. Numbers represent time in μs, and the white dashed lines denote the once-shocked interface.

region farther from IS_2 are more pronounced, they gradually move upstream with RW_1, separating away from IS_2. In the flow field adjacent to IS_2, the absolute values of E_p and E_ρ stay below 2 %, and those of E_u do not exceed 4 %. It is also evident that in all cases, the amplitude of the IS_2 wavefront is significantly smaller than that of the pre-reshock interface. These results indicate that assuming that the influence of the rippled RW_1 on IS_2 is negligible, i.e. IS_2 can be treated as a planar shock, in theoretical modelling, is reasonable.

C.2 *Non-uniformities in the flow field ahead of TS_2*

Similarly, to evaluate whether the interaction between TS_2 and the flow field ahead of it has a significant influence on the evolution of the twice-shocked interface, E_p, E_ρ and E_u are analysed. Here, p_0, ρ_0 and u_0 refer to the pressure, density and velocity in the region between TS_1 and TS_2 in simulations with a flat initial interface, respectively. The distributions of E_p, E_ρ and E_u shortly after reshock are presented in figure 17. It is observed that the absolute values of E_p and E_ρ do not exceed 1 %, and those of E_u remain

https://doi.org/10.1017/jfm.2025.10828 Published online by Cambridge University Press

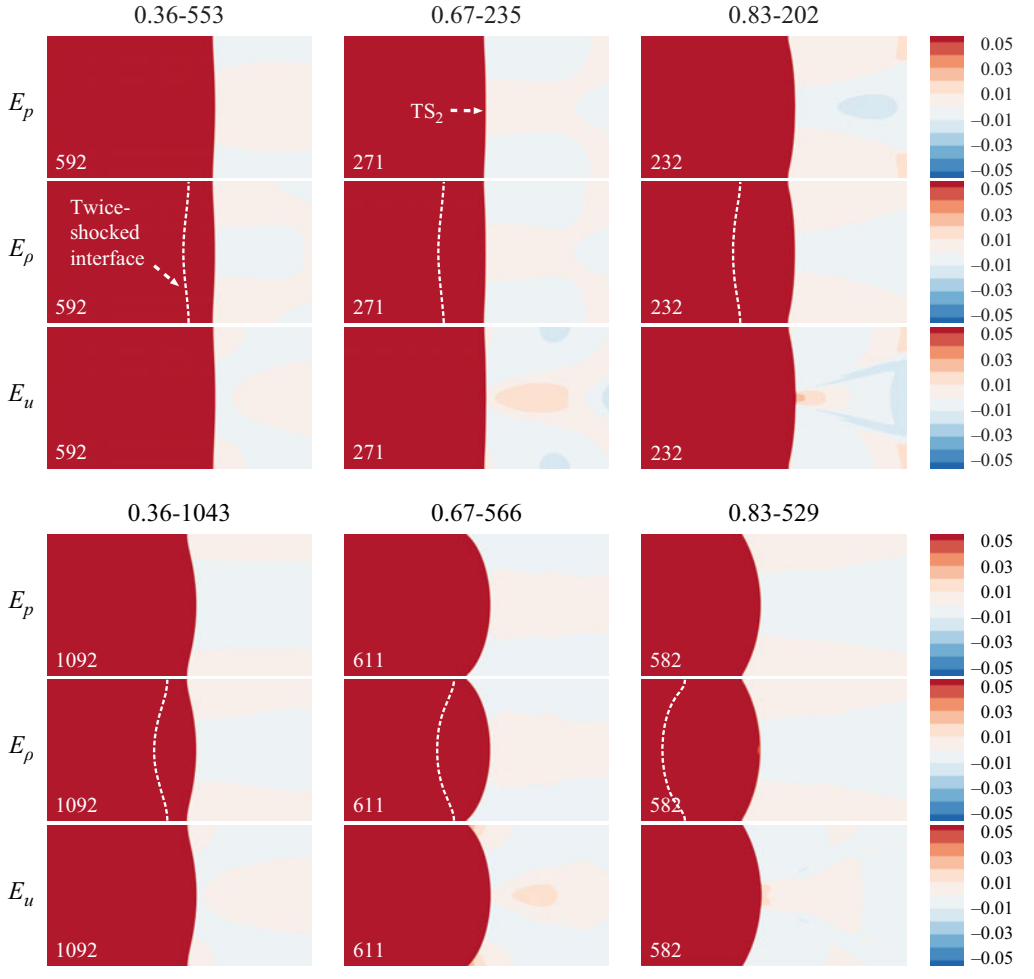


Figure 17. Distributions of E_p, E_ρ and E_u shortly after reshock. White dashed lines denote the twice-shocked interface.

below 2 % in the flow field adjacent to TS_2. Therefore, assuming that the non-uniformities in the flow field behind TS_1 have a negligible influence on TS_2, i.e. the flow field ahead of TS_2 can be approximated as uniform, in theoretical modelling, is reasonable.

References

Bell, G.I. 1951 Taylor instability on cylinders and spheres in the small amplitude approximation, *Tech. Rep.* LA-1321. LANL Los Alamos Scientific Laboratory of the University of California.

Betti, R. & Hurricane, O.A. 2016 Inertial-confinement fusion with lasers. *Nat. Phys.* **12**, 435–448.

Betti, R., Zhou, C.D., Anderson, K.S., Perkins, L.J., Theobald, W. & Solodov, A.A. 2007 Shock ignition of thermonuclear fuel with high areal density. *Phys. Rev. Lett.* **98**, 155001.

Cao, Q., Chen, C., Wang, H., Zhai, Z. & Luo, X. 2024 Interface evolution induced by two successive shocks under diverse reshock conditions. *J. Fluid Mech.* **999**, A31.

Charakhch'yan, A.A. 2000 Richtmyer–Meshkov instability of an interface between two media due to passage of two successive shocks. *J. Appl. Mech. Tech. Phys.* **41**, 23–31.

Charakhch'yan, A.A. 2001 Reshocking at the non-linear stage of Richtmyer–Meshkov instability. *Plasma Phys. Control. Fusion* **43**, 1169–1179.

Chen, C., Xing, Y., Wang, H., Zhai, Z. & Luo, X. 2023 Experimental study on Richtmyer–Meshkov instability at a light–heavy interface over a wide range of Atwood numbers. *J. Fluid Mech.* **975**, A29.

https://doi.org/10.1017/jfm.2025.10828 Published online by Cambridge University Press

CHERNE, F.J., HAMMERBERG, J.E., ANDREWS, M.J., KARKHANIS, V. & RAMAPRABHU, P. 2015 On shock driven jetting of liquid from non-sinusoidal surfaces into a vacuum. *J. Appl. Phys.* **118**, 185901.

DIMONTE, G. & RAMAPRABHU, P. 2010 Simulations and model of the nonlinear Richtmyer–Meshkov instability. *Phys. Fluids* **22**, 014104.

DING, J., LIANG, Y., CHEN, M., ZHAI, Z., SI, T. & LUO, X. 2018 Interaction of planar shock wave with three-dimensional heavy cylindrical bubble. *Phys. Fluids* **30**, 106109.

DING, J., SI, T., CHEN, M., ZHAI, Z., LU, X. & LUO, X. 2017*a* On the interaction of a planar shock with a three-dimensional light gas cylinder. *J. Fluid Mech.* **828**, 289–317.

DING, J., SI, T., YANG, J., LU, X., ZHAI, Z. & LUO, X. 2017*b* Measurement of a Richtmyer–Meshkov instability at an air–SF_6 interface in a semiannular shock tube. *Phys. Rev. Lett.* **119**, 014501.

FENG, L., XU, J., ZHAI, Z. & LUO, X. 2021 Evolution of shock-accelerated double-layer gas cylinder. *Phys. Fluids* **33**, 086105.

GONCHAROV, V.N., KNAUER, J.P., MCKENTY, P.W., RADHA, P.B., SANGSTER, T.C., SKUPSKY, S., BETTI, R., MCCRORY, R.L. & MEYERHOFER, D.D. 2003 Improved performance of direct-drive inertial confinement fusion target designs with adiabat shaping using an intensity picket. *Phys. Plasmas* **10**, 1906–1918.

HOLMES, R.L., DIMONTE, G., FRYXELL, B., GITTINGS, M.L., GROVE, J.W., SCHNEIDER, M., SHARP, D.H., VELIKOVICH, A.L., WEAVER, R.P. & ZHANG, Q. 1999 Richtmyer–Meshkov instability growth: experiment, simulation and theory. *J. Fluid Mech.* **389**, 55–79.

KARKHANIS, V. & RAMAPRABHU, P. 2019 Ejecta velocities in twice-shocked liquid metals under extreme conditions: A hydrodynamic approach. *Matter Radiat. Extremes* **4**, 044402.

KARKHANIS, V., RAMAPRABHU, P., BUTTLER, W.T., HAMMERBERG, J.E., CHERNE, F.J. & ANDREWS, M.J. 2017 Ejecta production from second shock: numerical simulations and experiments. *J. Dyn. Behav. Mater.* **3**, 265–279.

KRITCHER, A.L. *et al.* 2022 Design of inertial fusion implosions reaching the burning plasma regime. *Nat. Phys.* **18**, 251–258.

LI, J., CHEN, C., ZHAI, Z. & LUO, X. 2024 Effects of compressibility on Richtmyer–Meshkov instability of heavy/light interface. *Phys. Fluids* **36**, 056104.

LINDL, J., LANDEN, O., EDWARDS, J., MOSES, E., *et al.* 2014 Review of the National Ignition Campaign 2009–2012. *Phys. Plasmas* **21**, 020501.

LINDL, J.D., AMENDT, P., BERGER, R.L., GLENDINNING, S.G., GLENZER, S.H., HAAN, S.W., KAUFFMAN, R.L., LANDEN, O.L. & SUTER, L.J. 2004 The physics basis for ignition using indirect-drive targets on the National Ignition Facility. *Phys. Plasmas* **11**, 339–491.

LINDL, J.D., MCCRORY, R.L. & CAMPBELL, E.M. 1992 Progress toward ignition and burn propagation in inertial confinement fusion. *Phys. Today* **45**, 32–40.

LOMBARDINI, M. & PULLIN, D.I. 2009 Startup process in the Richtmyer–Meshkov instability. *Phys. Fluids* **21**, 044104.

LOMBARDINI, M., PULLIN, D.I. & MEIRON, D.I. 2014 Turbulent mixing driven by spherical implosions. Part 1. Flow description and mixing-layer growth. *J. Fluid Mech.* **748**, 85–112.

MERRITT, E.C. *et al.* 2023 Same-sided successive-shock HED instability experiments. *Phys. Plasmas* **30**, 072108.

MESHKOV, E.E. 1969 Instability of the interface of two gases accelerated by a shock wave. *Fluid Dyn.* **4**, 101–104.

MIKAELIAN, K.O. 1985 Richtmyer–Meshkov instabilities in stratified fluids. *Phys. Rev. A* **31**, 410–419.

MIKAELIAN, K.O. 1994 Freeze-out and the effect of compressibility in the Richtmyer–Meshkov instability. *Phys. Fluids* **6**, 356–368.

MIRELS, H. 1956 Boundary layer behind shock or thin expansion wave moving into stationary fluid. NACA Tech. Rep. (TN 3712 NACA).

MURAKAMI, M., NAGATOMO, H., AZECHI, H., OGANDO, F., PERLADO, M. & ELIEZER, S. 2006 Innovative ignition scheme for ICF-impact fast ignition. *Nucl. Fusion* **46**, 99–103.

NUCKOLLS, J., WOOD, L., THIESSEN, A. & ZIMMERMAN, G. 1972 Laser compression of matter to super-high densities: thermonuclear (CTR) applications. *Nature* **239**, 139–142.

PLESSET, M.S. 1954 On the stability of fluid flows with spherical symmetry. *J. Appl. Phys.* **25**, 96–98.

PROBYN, M.G., WILLIAMS, R.J.R., THORNBER, B., DRIKAKIS, D. & YOUNGS, D.L. 2021 2D single-mode Richtmyer–Meshkov instability. *Physica D* **418**, 132827.

RAYLEIGH, LORD 1883 Investigation of the character of the equilibrium of an incompressible heavy fluid of variable density. *Proc. Lond. Math. Soc.* **14**, 170–177.

RICHTMYER, R.D. 1960 Taylor instability in shock acceleration of compressible fluids. *Commun. Pure Appl. Math.* **13**, 297–319.

https://doi.org/10.1017/jfm.2025.10828 Published online by Cambridge University Press

RIKANATI, A., ORON, D., SADOT, O. & SHVARTS, D. 2003 High initial amplitude and high Mach number effects on the evolution of the single-mode Richtmyer–Meshkov instability. *Phys. Rev. E* **67**, 026307.

SAMULSKI, C., SRINIVASAN, B., MANUEL, M.J.E., MASTI, R.L., SAUPPE, J.P. & KLINE, J. 2022 Deceleration-stage Rayleigh–Taylor growth in a background magnetic field studied in cylindrical and Cartesian geometries. *Matt. Radiat. Extrem.* **7**, 026902.

SCHILL, W.J. *et al.* 2024 Suppression of Richtmyer–Meshkov instability via special pairs of shocks and phase transitions. *Phys. Rev. Lett.* **132**, 024001.

SI, T., JIANG, S., CAI, W., WANG, H. & LUO, X. 2025 Shock-tube experiments on strong-shock-driven single-mode Richtmyer–Meshkov instability. *J. Fluid Mech.* **1006**, R1.

TABAK, M., HAMMER, J., GLINSKY, M.E., KRUER, W.L., WILKS, S.C., WOODWORTH, J., CAMPBELL, E.M., PERRY, M.D. & MASON, R.J. 1994 Ignition and high gain with ultrapowerful lasers. *Phys. Plasmas* **1**, 1626–1634.

TAYLOR, G. 1950 The instability of liquid surfaces when accelerated in a direction perpendicular to their planes. I. *Proc. R. Soc. Lond. A* **201**, 192–196.

WANG, H., CAO, Q., CHEN, C., ZHAI, Z. & LUO, X. 2022 Experimental study on a light–heavy interface evolution induced by two successive shock waves. *J. Fluid Mech.* **953**, A15.

WANG, H., WANG, H., ZHAI, Z. & LUO, X. 2023*a* High-amplitude effect on Richtmyer–Meshkov instability at a single-mode heavy–light interface. *Phys. Fluids* **35**, 126107.

WANG, H., WANG, H., ZHAI, Z. & LUO, X. 2023*b* High-amplitude effect on single-mode Richtmyer–Meshkov instability of a light–heavy interface. *Phys. Fluids* **35**, 016106.

WOUCHUK, J.G. 2001 Growth rate of the Richtmyer–Meshkov instability when a rarefaction is reflected. *Phys. Plasmas* **8**, 2890–2907.

WOUCHUK, J.G. & NISHIHARA, K. 1997 Asymptotic growth in the linear Richtmyer–Meshkov instability. *Phys. Plasmas* **4**, 1028–1038.

XING, Y., CHEN, C., LI, J., WANG, H., ZHAI, Z. & LUO, X. 2025 Atwood-number dependence of the Richtmyer–Meshkov instability at a heavy–light single-mode interface. *J. Fluid Mech.* **1007**, A54.

YANG, Y., ZHANG, Q. & SHARP, D.H. 1994 Small amplitude theory of Richtmyer–Meshkov instability. *Phys. Fluids* **6**, 1856–1873.

ZHAI, Z., CHEN, C., XING, Y., LI, J., CAO, Q., WANG, H. & LUO, X. 2025 Manipulation of Richtmyer–Meshkov instability on a heavy–light interface via successive shocks. *J. Fluid Mech.* **1003**, A9.

ZHANG, J. *et al.* 2020 Double-cone ignition scheme for inertial confinement fusion. *Phil. Trans. R. Soc. A* **378**, 20200015.

ZHOU, Y. 2017*a* Rayleigh–Taylor and Richtmyer–Meshkov instability induced flow, turbulence, and mixing. I. *Phys. Rep.* **720–722**, 1–136.

ZHOU, Y. 2017*b* Rayleigh–Taylor and Richtmyer–Meshkov instability induced flow, turbulence, and mixing. II. *Phys. Rep.* **723–725**, 1–160.

ZHOU, Y. 2024 *Hydrodynamic Instabilities and Turbulence: Rayleigh–Taylor, Richtmyer–Meshkov, and Kelvin–Helmholtz Mixing*. Cambridge University Press.

ZHOU, Y., SADLER, J.D. & HURRICANE, O.A. 2025 Instabilities and mixing in inertial confinement fusion. *Annu. Rev. Fluid Mech.* **57**, 197–225.

ZHOU, Y. *et al.* 2019 Turbulent mixing and transition criteria of flows induced by hydrodynamic instabilities. *Phys. Plasmas* **26**, 080901.

ZHOU, Y. *et al.* 2021 Rayleigh–Taylor and Richtmyer–Meshkov instabilities: a journey through scales. *Physica D* **423**, 132838.

ZYLSTRA, A.B. *et al.* 2022 Burning plasma achieved in inertial fusion. *Nature* **601**, 542–548.

https://doi.org/10.1017/jfm.2025.10828 Published online by Cambridge University Press